HAL open science

A second gradient cohesive element for mode I crack propagation

Gwendal Jouan, Panagiotis Kotronis, Denis Caillerie, Frédéric Collin

To cite this version:

Gwendal Jouan, Panagiotis Kotronis, Denis Caillerie, Frédéric Collin. A second gradient cohesive element for mode I crack propagation. Finite Elements in Analysis and Design, 2022, 204, pp.103732. 10.1016/j.finel.2022.103732 . hal-03562970

HAL Id: hal-03562970

https://cnrs.hal.science/hal-03562970v1

Submitted on 11 Dec 2023

HAL is a multi-disciplinary open access archive for the deposit and dissemination of scientific research documents, whether they are published or not. The documents may come from teaching and research institutions in France or abroad, or from public or private research centers.

L'archive ouverte pluridisciplinaire **HAL**, est destinée au dépôt et à la diffusion de documents scientifiques de niveau recherche, publiés ou non, émanant des établissements d'enseignement et de recherche français ou étrangers, des laboratoires publics ou privés.

A second gradient cohesive element for mode I crack propagation

Gwendal JOUAN[a,c], Panagiotis KOTRONIS[a,*], Denis CAILLERIE[b], Frédéric COLLIN[c]

[a] *École Centrale de Nantes, Université de Nantes, CNRS*
Institut de Recherche en Génie Civil et Mécanique (GeM), UMR 6183
1 rue de la Noë, BP 92101, 44321, Nantes, cedex 3, France
[b] *University Grenoble Alpes, CNRS, Grenoble INP, 3SR, F-38000, Grenoble, France*
[c] *ArGEnCo Department, University of Liège,*
Allée de la Découverte 9, 4000 Liège, Belgium

Abstract

Modeling strain localization with a second gradient model can become problematic at the late stages of softening response, when the second gradient terms become significant compared to the first gradient terms. This is particularly true for mode I crack problems where an unrealistic spreading of the localised zone can be encountered. To deal with these limitations, a novel second gradient interface element for mode I crack propagation problems is introduced. It is shown that the model is able to correctly reproduce all the different phases up to failure; the adherence phase, strain localisation, the transition from localised strains to cohesive zones and full crack opening.

Keywords: second gradient; strain localization; regularization; cohesive element; higher-order continua; micromorphic continua; generalized continua; crack; transition

1. Introduction

Two approaches are often used to simulate cracks in quasi-brittle materials : a purely continuous approach, often within the framework of damage mechanics [1] [2] and a discontinuous approach, mainly based on fracture mechanics [3] [4] [5]. In the former, the solid remains a continuum while the failure process is described by a damage field that governs the softening response of the material. This approach necessitates the introduction of a length scale to avoid ill-posedness and spurious localization of the damage and strain fields (regularization). Among the various regularization methods in the continuum mechanics approach, this article deals with the so called micromorphic or generalized continua [6] [7] [8] that take into account a kinematic description of the microstructure. In the latter, cracks are naturally described by displacement discontinuities. In its simplest form, linear elastic fracture mechanics, the material outside the crack is assumed linear elastic while an energy criterion is adopted to predict crack initiation. Cohesive zone models [9] [10] [11], which can be considered as an extension of the Griffith's fracture mechanics theory [12], are used to simulate crack initiation and propagation. The transition from diffuse material degradation to a localized crack is still however a challenging problem [13], especially if the crack path is not known in advance or if multiple cracks are present.

*Corresponding author
Email address: `Panagiotis.Kotronis@ec-nantes.fr` (Panagiotis KOTRONIS)

One particular type of generalized continua, the second gradient model developed by Chambon et al. [14] [15] [16] [17], has demonstrated its ability to regularize strain localization in the framework of plasticity [15] [18] [19] and damage mechanics [2] [20] [21]. Shear banding problems [22] [23] [24] [25] and mode I crack propagation [2] can be reproduced up to a certain point.

On the other hand, as demonstrated by various authors [21] [26] [27] [28] [29], strain localization with a second gradient model can become problematic at the late stages of softening response, when the second gradient terms become significant compared to the first gradient terms. This is particularly true for sharp or narrow mode I fracture problems where high values of damage are expected as soon as the crack starts propagating. An unrealistic spreading of the damaged zone can be encountered due to the significant values of the second gradient terms used in equilibrium equations. So the forces transmitted through the localization zone are important even for high damage values. Similar issues occurs with other regularization techniques; for example, the widening of the damage zone is a well known problem for the non-local - and the closely related implicit gradient, damage models [30] [31]. Additional issues associated with the numerical implementation of the regularization methods may also occur, such as the narrowing of the localization band below the finite element size [3]. Recent formulations, as the gradient damage model proposed by Zhao Wang & Leong Hien Poh [32] or phase field fracture models seem to overcome these problems. One can also mention the hemivariational continuum approach proposed in [33] to reproduce damage induced anisotropy, chirality and formation of finite localization zones.

In this article however we focus on the second gradient model developed by Chambon et al. [14] [15] [16] [17] because of its versatility, as it is able to simulate strain localization within different constitutive law frameworks (plasticity, hypoplasticity, viscoplasticity, damage mechanics etc). No additional modification of the finite element software is needed other than the implementation of the second gradient finite element; all the implemented constitutive laws can be used straightforwardly. Furthermore, an extension of the formulation for poromechanical modeling is introduced in [25] and has already proved its performance (see among others [34], [35], [36]).

To simulate crack opening and propagation, various authors studied the introduction of discontinuities in continuous damage models [3] [4] [5] [37] [38] [39] [40]. Discontinuities are generally introduced at points where damage reaches a critical value while strain localization and damage fields can evolve elsewhere in the structure. This critical value corresponds either to a complete rupture of the material and in this case the inserted discontinuity is traction free, or to any other value that implies the use of a cohesive zone model to deal with the remaining energy that has yet to be dissipated during the crack formation.

The objective of this article is to study mode I crack propagation problems and the transition from continuous damage to a cohesive zone in a second gradient continuum. The article is divided into two parts: the first part (sections 2 and 3) presents the second gradient formulation (virtual work principle, constitutive laws and numerical implementation issues) and focuses on two examples to illustrate the spurious behavior that can be encountered. The second part (section 4) introduces a solution, a second gradient cohesive element (virtual

work principle, numerical implementation) and ends with two examples to validate the approach.

The following notations are adopted hereafter: the upper script * represents a virtual variable, the $'$ and $''$ the first and second derivative with respect to the coordinate x, ∇ the gradient, ∇^2 the second gradient, : the double contraction, $\therefore$ the triple contraction, $\otimes$ the tensor product and div the divergence operator respectively. $\underline{q}$ is a first order tensor (vector), $\underline{n}$ the unit surface normal vector, $\underline{\underline{q}}$ a second order tensor, $\overline{q}$ a third order tensor and $\overline{\overline{q}}$ a fourth order tensor. The partial derivatives are denoted as $q_{i,j} = \partial q_i/\partial x_j$, $q_{i,jk} = \partial^2 q_i/\partial x_j \partial x_k$. Dq is the normal derivative of any quantity q (i.e. $Dq = (\frac{\partial q}{\partial x_k})n_k$) and $\frac{Dq}{Dx_j}$ is the tangential derivative of any quantity q (i.e. $\frac{Dq}{Dx_j} = \frac{\partial q}{\partial x_j} - (\frac{\partial q}{\partial x_k})n_k n_j$). The normal and tangential components of a vector are given as $q_i = (q_i)_t + q_l n_l n_i$, with $(q_i)_t$ the tangential component. The normal and tangential components of a second order tensor are given as $q_{ij} = (q_{ij})_t + q_{il} n_l n_j$ with $(q_{ij})_t$ the tangential component. Body forces are hereafter neglected for simplicity and inertia phenomena are not taken into account.

2. The second gradient model

2.1. Virtual work principle

As shown by Germain [6] (see also [14] [15]), second gradient continua can be seen as a particular case of micromorphic or generalized continua. This type of continua introduces a kinematic of the microstructure via a tensor $\underline{\underline{v}}$. In the second gradient model introduced in [15], the tensor $\underline{\underline{v}}$ represents the micro strains and is supposed equal to the macro strains $\nabla \underline{u}$, where $\underline{u}$ is the macro displacement field. That feature holds true as far as bulk equations are concerned, however boundary conditions for second grade continua present particularities with regard to those of micromorphic continua.

The virtual work principle for second grade continua is given by:

$$\int_\Omega (\underline{\underline{\sigma}} : \nabla \underline{u}^* + \overline{\Sigma} \therefore \nabla^2 \underline{u}^*) d\Omega = \int_{\partial\Omega} (\underline{s}.\underline{u}^* + \underline{T}.D\underline{u}^*) d\Gamma \tag{1}$$

which is the weak formulation of equilibrium.

On the boundary $\partial\Omega$, $\underline{u}^*$ and its normal derivative $D\underline{u}^*$ vary independently, the force densities $\underline{s}$ and $\underline{T}$ (dual to the normal derivative of $\underline{u}$) can be also chosen independently [15].

Using the virtual work principle (equation (1)), several integration by parts and the divergence theorem finally provides the following balance equations and boundary conditions [15]:

$$div(\underline{\underline{\sigma}} - div(\overline{\Sigma})) = 0 \tag{2}$$

$$\frac{\partial \sigma_{ij}}{\partial x_j} - \frac{\partial^2 \Sigma_{ijk}}{\partial x_j \partial x_k} = 0 \tag{3}$$

Under the assumption of smooth boundary (without edges or corners), the boundary equations become (the existence of corners necessitates the introduction of additional terms):

$$\sigma_{ij} n_j - n_k n_j D\Sigma_{ijk} - \frac{D\Sigma_{ijk}}{Dx_k} n_j - \frac{D\Sigma_{ijk}}{Dx_j} n_k + \frac{Dn_l}{Dx_l} \Sigma_{ijk} n_j n_k - \frac{Dn_j}{Dx_k} \Sigma_{ijk} = s_i \tag{4}$$

$$\Sigma_{ijk} n_j n_k = T_i \tag{5}$$

2.2. Constitutive laws

The introduction of the second gradient of the displacements and its dual double stress tensor (equation 1) in the internal virtual work implies different possibilities regarding the constitutive laws linking the two stress tensors and the displacement gradients [41]. The choice made by Chambon and co-workers [15] [18], adopted also in this article, is to decouple the first and the second gradient constitutive laws, i.e. the first gradient stress tensor $\underline{\underline{\sigma}}$ is a function of $\nabla \underline{u}$ and the double stress $\overline{\Sigma}$ a function of $\nabla^2 \underline{u}$.

2.2.1. First gradient part

A simple damage mechanic law is adopted in this article for the constitutive law of the first gradient part, equation (6). The law has a scalar damage variable $\mathbb{D}$, function of an internal variable κ depending on the load history and on the equivalent strain ϵ_{eq} through the definition of a loading function, equation (7) and the Kuhn-Tucker conditions, equation (8) :

$$\underline{\underline{\sigma}} = (1 - \mathbb{D}(\kappa))\overline{\overline{E}} \nabla \underline{u} \tag{6}$$

$$f(\epsilon_{eq}, \kappa) = \epsilon_{eq} - \kappa \tag{7}$$

$$f \leq 0; \quad \dot{\kappa} \geq 0; \quad f\dot{\kappa} = 0 \tag{8}$$

The definition of the equivalent strain and the damage evolution law, which provides $\mathbb{D}$ as a function of κ, are detailed in section 3.

2.2.2. Second gradient part

The constitutive law for the second gradient part is chosen linear elastic. Following Mindlin [42] [8] it is written in 2D as:

$$\begin{Bmatrix} \Sigma_{111} \\ \Sigma_{112} \\ \Sigma_{121} \\ \Sigma_{122} \\ \Sigma_{211} \\ \Sigma_{212} \\ \Sigma_{221} \\ \Sigma_{222} \end{Bmatrix} = \begin{bmatrix} \alpha^{12345} & 0 & 0 & \alpha^{23} & 0 & \alpha^{12} & \alpha^{12} & 0 \\ 0 & \alpha^{145} & \alpha^{145} & 0 & \alpha^{25} & 0 & 0 & \alpha^{12} \\ 0 & \alpha^{145} & \alpha^{145} & 0 & \alpha^{25} & 0 & 0 & \alpha^{12} \\ \alpha^{23} & 0 & 0 & \alpha^{34} & 0 & \alpha^{25} & \alpha^{25} & 0 \\ 0 & \alpha^{25} & \alpha^{25} & 0 & \alpha^{34} & 0 & 0 & \alpha^{23} \\ \alpha^{12} & 0 & 0 & \alpha^{25} & 0 & \alpha^{145} & \alpha^{145} & 0 \\ \alpha^{12} & 0 & 0 & \alpha^{25} & 0 & \alpha^{145} & \alpha^{145} & 0 \\ 0 & \alpha^{12} & \alpha^{12} & 0 & \alpha^{23} & 0 & 0 & \alpha^{12345} \end{bmatrix} \begin{Bmatrix} u_{1,11} \\ u_{1,12} \\ u_{1,21} \\ u_{1,22} \\ u_{2,11} \\ u_{2,12} \\ u_{2,21} \\ u_{2,22} \end{Bmatrix}, \tag{9}$$

where :

$$
\begin{aligned}
\alpha^{12345} &= 2(\alpha^1 + \alpha^2 + \alpha^3 + \alpha^4 + \alpha^5), \\
\alpha^{23} &= \alpha^2 + 2\alpha^3, \\
\alpha^{12} &= \alpha^1 + \alpha^2/2, \\
\alpha^{145} &= \alpha^1/2 + \alpha^4 + \alpha^5/2, \\
\alpha^{25} &= \alpha^2/2 + \alpha^5, \\
\alpha^{34} &= 2(\alpha^3 + 2\alpha^4).
\end{aligned} \tag{10}
$$

with $\alpha^1, \alpha^2, \alpha^3, \alpha^4, \alpha^5$ five independent material parameters.

As in Matsushima et al [18], the choice here is to work only with one independent material parameter B, as this was proven sufficient to regularize various localization problems [18] [19] [23]:

$$
\begin{aligned}
a_1 &= 0 \\
a_2 &= B \\
a_3 &= -B/2 \\
a_4 &= B \\
a_5 &= -B
\end{aligned} \tag{11}
$$

The linear elastic constitutive law of the second gradient part is finally given by :

$$
\begin{Bmatrix} \Sigma_{111} \\ \Sigma_{112} \\ \Sigma_{121} \\ \Sigma_{122} \\ \Sigma_{211} \\ \Sigma_{212} \\ \Sigma_{221} \\ \Sigma_{222} \end{Bmatrix}
=
\begin{bmatrix}
B & 0 & 0 & 0 & 0 & B/2 & B/2 & 0 \\
0 & B/2 & B/2 & 0 & -B/2 & 0 & 0 & B/2 \\
0 & B/2 & B/2 & 0 & -B/2 & 0 & 0 & B/2 \\
0 & 0 & 0 & B & 0 & -B/2 & -B/2 & 0 \\
0 & -B/2 & -B/2 & 0 & B & 0 & 0 & 0 \\
B/2 & 0 & 0 & -B/2 & 0 & B/2 & B/2 & 0 \\
B/2 & 0 & 0 & -B/2 & 0 & B/2 & B/2 & 0 \\
0 & B/2 & B/2 & 0 & 0 & 0 & 0 & B
\end{bmatrix}
\begin{Bmatrix} u_{1,11} \\ u_{1,12} \\ u_{1,21} \\ u_{1,22} \\ u_{2,11} \\ u_{2,12} \\ u_{2,21} \\ u_{2,22} \end{Bmatrix}. \tag{12}
$$

It should be noted however that the different elastic material parameters for the second gradient constitutive law can be obtained by a homogenization procedure over a representative volume element (see for example [43] [44] [45]). A generalized Hooke's law for isotropic second gradient materials characterized by seven elastic moduli is proposed in [46].

2.3. Finite element mixed formulation

The virtual work form of equation (1) introduces derivatives of the second order for the displacement field and thus necessitates functions of class $C1$ (continuous and continuously differentiable once) for its interpolation [47]. Such finite element has been used for $1D$ problems by Chambon et al. [14] but is difficult to construct for $2D$ and $3D$ cases (see however [48] and [49]). For this numerical reason, it is more convenient to use the weak formulation of the equilibrium of a general micromorphic continuum (see appendix Eq.A.9 for more details) that can be used to numerically model the deformations of a second gradient continuum. In that case, one

uses two virtual fields $\underline{u}^*$ and $\underline{\underline{v}}^*$ that necessitate functions of class $C0$ (continuous). However, it is necessary to force the micro strain $\underline{\underline{v}}$ to be equal to the gradient $\nabla\underline{u}$ of the displacement field. Consequently Lagrange multipliers (namely $\underline{\underline{\tau}}$ and $\underline{\underline{P}}_t$ defined in the Appendix A) are necessary to impose the kinematic constraint $\underline{\underline{v}} = \nabla\underline{u}$ respectively on the domain and its boundary. They are unknowns and cannot be fixed as data nor given by a constitutive equation.

To impose the equality of the microstrains and the macrostrains the virtual work principle takes the following form [15], [50]:

$$\int_\Omega (\underline{\underline{\sigma}} : \nabla\underline{u}^* + \underline{\underline{\lambda}} : (\underline{\underline{v}}^* - \nabla\underline{u}^*) + \overline{\Sigma} \therefore \nabla\underline{\underline{v}}^* d\Omega = \int_\Gamma \left(\underline{s}.\ \underline{u}^* + \underline{P}_n : \underline{v}_n^* + \underline{\underline{\rho}} : \left(\underline{\underline{v}}_t^* - \nabla_t\underline{u}^*\right)\right) d\Gamma \tag{13}$$

and

$$-\int_\Omega \underline{\underline{\lambda}}^* : (\underline{\underline{v}} - \nabla\underline{u}) d\Omega = 0 \tag{14}$$

and

$$\int_\Gamma \underline{\underline{\rho}}^* : (\underline{\underline{v}}_t - \nabla_t\underline{u}) d\Gamma = 0 \tag{15}$$

which holds for any admissible fields $\underline{u}^*$, $\underline{\underline{v}}^*$, $\underline{\underline{\lambda}}^*$ and $\underline{\underline{\rho}}^*$. From equations (A.9) and (13) one can also observe that the Lagrange multiplier field $\underline{\underline{\lambda}}$ is equivalent to the micro stress tensor $\underline{\underline{\tau}}$ and the Lagrange multiplier field $\underline{\underline{\rho}}$ equal to $\underline{\underline{P}}_t$. $\underline{s}$ is the external surface force and $\underline{P}_n$ is the external double force that can be chosen independently.

The success of the finite element formulation depends upon the behavior of the Lagrange multiplier field. In the following, this is considered constant on each finite element [15] [17] [18], as this is the best choice in terms of computational cost [24]. Nevertheless, the use of constant Lagrange multipliers alone can introduce spurious oscillations (e.g. in mode I crack propagation problems [21] [28]). The kinematic constraint of the second gradient model can be also imposed with a penalty method, by specifying a "constitutive law" for $\underline{\underline{\tau}}$ of the form [24] [51]:

$$\underline{\underline{\tau}} = C(\nabla\underline{u} - \underline{\underline{v}}) \tag{16}$$

where C is the (scalar) penalty coefficient which must be taken as large as possible to correctly enforce the equality. In the second gradient model however it is very difficult to choose the appropriate value for the penalization parameter, which in fact has to be very large [24]. The combined use of Lagrange multiplier fields and penalization terms is a way out, as it improves the convergence performance and the sensitivity to the value of the penalization parameter [21] [24] [28]. In this latter case, Eq.13 becomes:

$$\int_\Omega (\underline{\underline{\sigma}} : \nabla\underline{u}^* + (\underline{\underline{\lambda}} + \underline{\underline{\tau}}) : (\underline{\underline{v}}^* - \nabla\underline{u}^*) + \overline{\Sigma} \therefore \nabla\underline{\underline{v}}^* d\Omega = \int_\Gamma \left(\underline{s}.\ \underline{u}^* + \underline{P}_n : \underline{v}_n^* + \underline{\underline{\rho}} : \left(\underline{\underline{v}}_t^* - \nabla_t\underline{u}^*\right)\right) d\Gamma \tag{17}$$

Other choices of the Lagrange multiplier field are also possible [52] but it is necessary to verify that they satisfy they Ladyzhenskaya–Babuška–Brezzi (LBB) condition [53]. One can for example mention the use of a

linear field for the Lagrange multipliers for the specific case of the second gradient model for dilatant materials, in the mixed formulation introduced by [54], that does not need the use of penalization terms to correctly reproduce the incompressible material behavior.

The additional term $(\underline{\underline{v}}_t - \nabla_t \underline{u})$ in the virtual work principle for the external forces on the surface Γ vanishes when the kinematic condition is fully respected and may be considered negligible when it is introduced in a weak way. On the parts of the surface Γ where the boundary conditions specify the displacement field and its gradient (forces and double surface forces are unknown), in order to guarantee the cancellation of the additional term, it is necessary to specify them as:

$$\underline{u} = \underline{u}^{imp} \quad \text{and} \quad \underline{\underline{v}} = \underline{v}_n^{imp} \otimes \underline{n} + \nabla_t \underline{u}^{imp} \tag{18}$$

where the imposed $\underline{u}^{imp}$ and $\underline{v}_n^{imp}$ are specified independently and $\nabla_t \underline{u}^{imp}$ is deduced from the given imposed displacement $\underline{u}^{imp}$. Consequently, when one component of the displacement field $\underline{u}$ is fixed along a boundary, the component of $\underline{v}$ corresponding to the tangential derivative of the fixed displacement must be also fixed.

3. The second gradient theory as a regularization method for quasi-brittle damage problems

3.1. One-dimensional tensile problem

In their first paper on the second gradient theory (used as a regularization method for strain localization), Chambon and co-workers gave the closed form solution of a $1D$ traction problem [14]. Their results will be used hereafter to highlight some features of the model.

Let's consider a $1D$ bar of length L. An horizontal monotonically increasing displacement (tension) $u = U$ is applied at the right end of the bar while its left end is fixed $u = 0$. Zero double forces are considered at its both ends (figure 1(a)). In [14], a plastic $1D$ bilinear law was adopted for the first gradient part. The authors found that no unloading occurs inside the localization band and so it is possible to adopt the same bilinear constitutive law formulated within a damage mechanics framework. The following constitutive law is therefore adopted in this paper:

$$\mathbb{D} = \frac{\kappa_c}{\epsilon_{eq}} \frac{\epsilon_{eq} - \kappa_i}{\kappa_c - \kappa_i} \tag{19}$$

with ϵ_{eq} is the equivalent strain, κ_i the strain threshold at the peak of the bilinear law corresponding to the damage initiation and κ_c the strain threshold after which stresses are no longer transmitted. The equivalent strain is simply taken as $\epsilon_{eq} = \epsilon = u'$. The initial slope of the first gradient law is named G_{el} and the post damage slope $G_{tg} = \frac{G_{el}\kappa_i}{\kappa_i - \kappa_c}$. The second gradient law is the one dimensional version of (12) with a constant slope B linking the double stress Σ along the $1D$ bar with the second derivative of the displacements u'' (figure 1(b)).

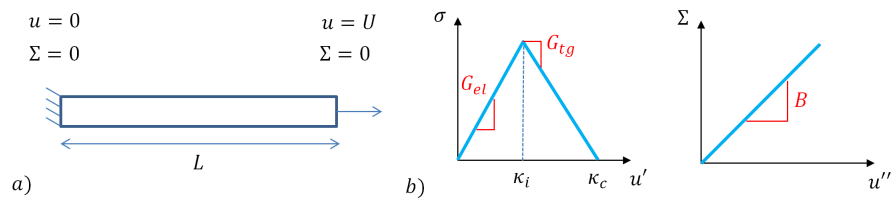

Figure 1: One-dimensional tensile test : Boundary conditions and constitutive laws

The balance equation (3) simply becomes:

$$\sigma' - \Sigma'' = 0 \tag{20}$$

and can be integrated as (with s the classical tensile traction):

$$\sigma - \Sigma' = s \tag{21}$$

Equation 20 is solved considering either a sound (undamaged) or damaged behavior. In the sound parts (i.e subdomain where $u' < \kappa_i$) the displacement is given by [14]:

$$u = \frac{s}{G_{el}}x + K + \alpha cosh(\omega x) + \beta sinh(\omega x) \tag{22}$$

In damaged parts (where $\kappa_i < u' < \kappa_c$), the displacement is given by [14]:

$$u = \frac{N_2}{G_{tg}}x + Q + \gamma cos(\eta x) + \delta sin(\eta x) \tag{23}$$

with

$$\eta = \sqrt{\frac{-G_{tg}}{B}} \tag{24}$$

$$\omega = \sqrt{\frac{G_{el}}{B}} \tag{25}$$

$$N_2 = s + (G_{tg} - G_{el})u' \tag{26}$$

and α, β, γ, Q, K constants.

A various number of damaged and sound subdomains can be "linked" together, and thus several solutions to the boundary problem are possible with a different number of "damaged" and "sound" parts. The total number of solution is finite and depends on the boundary conditions and the material parameters [14]. The localization length (the total length of the soft parts l_s) can be approximated by the wave-length λ_s [14] and it is obvious from equation (27) that for a bigger value of B the length of the localization zone increases:

$$l_s \simeq \lambda_s = 2\pi\sqrt{\frac{-B}{G_{tg}}} \tag{27}$$

The solution given in [14] is valid as long as $u' < \kappa_c$ (i.e. $\sigma > 0$) everywhere.

It is important to keep in mind that, in a second gradient continuum, the traction applied at the boundary is balanced by both stress and double stress quantities (equation (21)), meaning that σ is not necessarily constant along the $1D$ bar. It is thus possible to have $\sigma = 0$ at one point (i.e. damage equal to 1), or even on a subdomain of the bar, while a tensile force is still transmitted. In this particular case, the closed form solution is no longer valid for $u' > \kappa_c$ (Figure 2). Rolshoven [26], Jirasek and Rolshoven [29] and [20] [2] [22] [27] [28] showed that this situation leads to an increasing localization zone that finally covers the whole length of the bar.

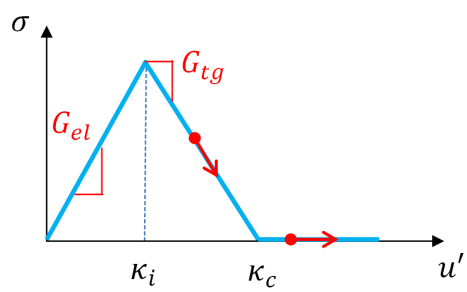

Figure 2: One-dimensional tensile test : the closed form solution is not valid for $u' > \kappa_c$

3.1.1. Tensile traction, stress and double stress

In order to have a better insight in the stress, double stress distribution and tensile traction evolution, these quantities are plotted as a function of the imposed displacement (the adopted parameters are given in table 1). One particular possible solution is studied, the "sound-damaged-sound" solution shown in Figure 3(a). In this case, the length of the sound part is $l_h = 2l_{h,end}$, while the length of the damaged part l_s can be found from the following equation [14]:

Type	Parameters		Value	Unit
Dimension	Length	L	1	m
First gradient law	Elastic Modulus	G^{el}	150	Pa
	Tangent modulus	G^{tg}	-75	Pa
	Strain limit	κ_i	0.01	-
Second gradient law	Elastic modulus	B	0.8	N

Table 1: One-dimensional tensile problem : Parameters

$$tanh\left(\omega\frac{L-l_s}{2}\right) = -\sqrt{\frac{-G_{el}}{G^{tg}}}tanh\left(\eta\frac{l_s}{2}\right) \tag{28}$$

Remark: this solution is equivalent to the "damaged-sound-damaged" solution in Figure 3(b), as both correspond to the same localization length and force displacement curve. In this case, $l_s = 2l_{s,end}$.

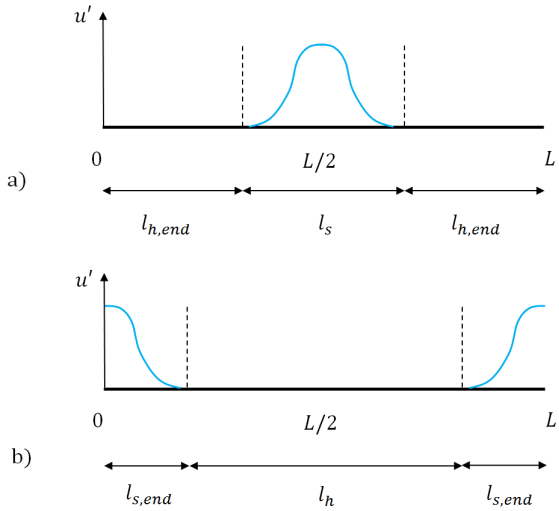

Figure 3: One-dimensional tensile test : a) "sound-damaged-sound" solution b) "damaged-sound-damaged" solution

From the closed form solution given in [14], the stress σ and the double stress Σ can be computed at any point in the bar using the displacement solution, the constitutive laws and the balance equation. The corresponding tensile traction s is finally given by [28]:

$$s = \frac{U + \frac{G_{el}-G_{tg}}{G_{tg}}\kappa_i l_s - \left(\frac{1}{\omega^2}+\frac{1}{\eta^2}\right)\omega\kappa_i tanh(\omega l_h)}{\frac{l_h}{G_{el}} + \frac{l_s}{G_{tg}} - \left(\frac{1}{\omega^2}+\frac{1}{\eta^2}\right)\frac{\omega}{G_{el}}tanh(\omega l_h)} \tag{29}$$

and the stress and Σ' at the maximum strain point ($x = L/2$) [28] are given as:

$$\sigma = G_{el}(\frac{N_2}{G_{tg}} + \zeta\eta) \tag{30}$$

$$-\Sigma' = B\zeta\eta^3 \tag{31}$$

with

$$\zeta = \frac{\kappa_i - \frac{N_2}{G_{tg}}}{\eta cos(\eta l_{s,end})} \tag{32}$$

s, σ and Σ' are hereafter adimensionalized with: $\tilde{\bullet} = \bullet/(G_{el}\kappa_i)$. The adimensionalized quantities depend on ω, η, L and are linear functions of the adimensionalized displacement $\tilde{U} = U/(L\kappa_i)$. The evolution of these quantities at the point of maximum strain (beginning of the bar for the damaged-sound-damaged solution or middle of the bar for the sound-damaged-sound case) is given in figure 4. When $\tilde{\sigma}$ becomes equal to zero, $\tilde{\Sigma}'$ is different from zero and therefore the transmitted tensile traction $\tilde{s}$ is not nul.

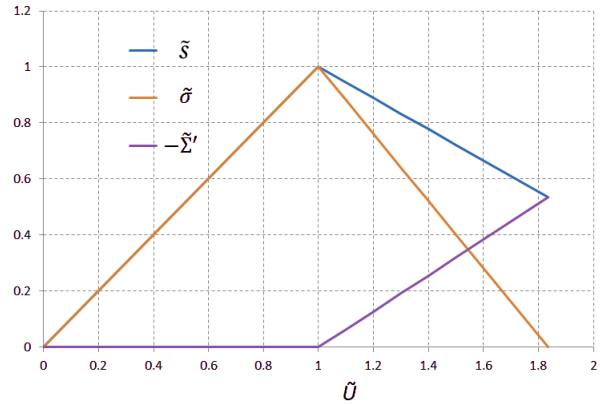

Figure 4: One-dimensional tensile test : Adimensionalized tensile traction $\tilde{s}$, stress $\tilde{\sigma}$ and $\tilde{\Sigma}'$ evolutions at the point of maximum strain with $\omega = 13.7m^{-1}$ and $\eta = 9.7m^{-1}$

The closed form solution is valid only up to the point where σ reaches 0 ($u' = \kappa_c$ at the point of maximum strain). Beyond this point, the localization length starts increasing. The limit value of $\tilde{s}$ obtained when damage reaches 1 is given by [28]:

$$\tilde{s}_{lim} = \frac{1}{1 - cos(\eta l_{s,end})} \tag{33}$$

Equation (33) indicates that for the constitutive laws adopted (figure 1) and when damage reaches 1, the adimensionalized tensile force in the bar cannot be less than half the maximum adimensionalized traction. This can be also observed in Figure 5 that gives the value of $\tilde{s}_{lim}$ for different values of η and ω, ($L = 1m$). This is clearly a non realistic behavior as the bar should be traction free if a crack appears and the bar is cut in pieces (see also sections 3.2 and 4).

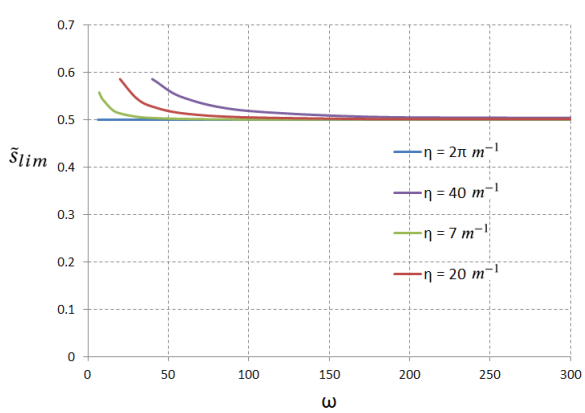

Figure 5: One-dimensional tensile test : Evolution of $\tilde{s}_{lim}$ as a function of η and ω ($L = 1m$)

Remarks:

- A way to solve the spurious spreading of the localization zone is to couple the first and second gradient constitutive laws so as to decrease the influence of the second gradient terms at the late loading stages. A 1D example using a damage mechanics formulation is presented in [27], where it is shown that a proper coupling can lead to a formulation able to a priori control the evolution (decrease, constant or increase) of the localization zone. Nevertheless and as it is shown in the 1D example in this section, the tensile force cannot become zero but presents a minimum. This is clearly a problem for crack modeling studies, which is solved in section 4 with the introduction of a second gradient cohesive element.

- The damage process could also result in introduction of new microstructures leading to growth or decrement of second gradient terms when compared to the first gradient terms. Thus spreading could be realistic in some cases, see for example [55] [56] [57].

3.1.2. Dissipated energy

The energy dissipated up to the point where damage reaches 1 can be calculated from the closed form solution. For a damage model, the dissipated energy on a domain Ω is given by :

$$G_f = \int_\Omega \int_0^{\mathbb{D}} Y d\mathbb{D} dx \tag{34}$$

with Y the energy release rate.

In our case, because damage is applied only to elastic modulus of the first gradient part, Y is the same as in a first gradient continuum. We thus have for the $1D$ problem:

$$Y = \frac{1}{2} G_{el} u'^2 \tag{35}$$

Considering the damage evolution law given by equation (19) and a monotonic loading we have:

$$d\mathbb{D} = \frac{\partial \mathbb{D}}{\partial \epsilon} d\epsilon = \frac{\partial \mathbb{D}}{\partial u'} du' = \frac{1}{u'^2} \frac{\kappa_i \kappa_c}{\kappa_c - \kappa_i} du' \tag{36}$$

For the "damaged-sound-damaged" solution, damage spreads at the two extremities of the bar ($l_s = 2l_{s,end}$) (see figure 3(b)). Equation (34) therefore becomes :

$$\frac{G_f}{2} = \int_0^{l_{s,end}} \int_{\kappa_i}^{u'(x)} \frac{1}{2} G_{el} \frac{\kappa_i \kappa_c}{\kappa_c - \kappa_i} du' dx = \int_0^{l_{s,end}} \frac{1}{2} G_{el} \frac{\kappa_i \kappa_c}{\kappa_c - \kappa_i} (u'(x) - \kappa_i) dx \tag{37}$$

where $u'(x)$ is calculated from equation (23) with the boundary conditions $u(0) = 0$, $\Sigma(0) = 0$ and $u'(l_{s,end}) = \kappa_i$:

$$u'(x) = \frac{t + (G_{tg} - G_{el})\kappa_i}{G_{tg}} + \frac{\kappa_i - \frac{N_2}{G_{tg}}}{\eta cos(\eta l_{s,end}} \eta cos(\eta x) \tag{38}$$

When damage reaches 1, the value of the tensile traction is given by equation (33). Equation (37) finally becomes [28]:

$$G_f = \frac{(G_{el} - G_{tg})G_{el}\kappa_i^2}{G_{tg}} \left[l_{s,end} \left(\frac{cos(\eta l_{s,end})}{1 - cos(\eta l_{s,end})} \right) - \frac{1}{\eta tan(\eta l_{s,end}/2)} \right] \tag{39}$$

The dissipated energy is therefore linked to the second gradient modulus B through $l_{s,end}$ and η. Equation (39) provides the energy dissipated up to the state when damage reaches 1 at the center of the process zone. Although this is not the state of complete failure and therefore this energy is not the fracture energy, equation (39) can be used for a first calibration of B.

3.2. Two-dimensional mode I crack propagation problem

Up to this point, the behavior of the second gradient model and several analytical results for the $1D$ tensile test have been presented. This simple case highlights some of the current limitations of the second gradient model used as a regularization model for strain localization.

The above limitations can be less or more severe depending of the crack propagation mode. For example, the second gradient model works very well for shear band problems, as already shown in various articles in the literature [22] [23] [24] [25]. Its performance is however less satisfying for mode I crack propagation problems (where damage increases rapidly and becomes close to 1). To illustrate this behavior, a notched trapezoidal beam with an imposed displacement at its lips [21] [5] is modeled hereafter, Figure 6.

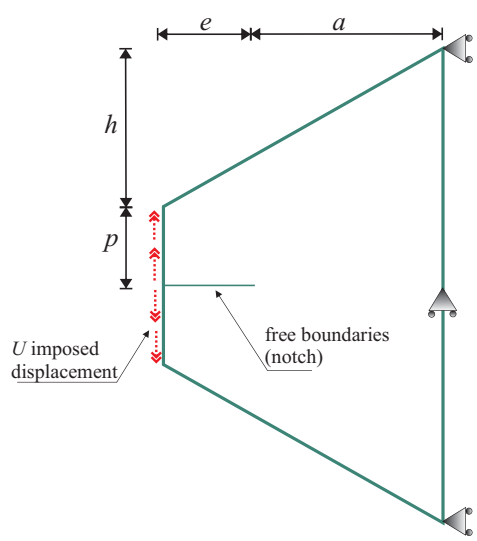

Figure 6: Mode I crack propagation test : Geometry

The damage evolution law is the same as in the $1D$ test (equation (19)). To obtain a mode I crack propagation the classical Mazars equivalent strain is adopted [58] as:

$$\epsilon_{eq} = \sqrt{\sum < \epsilon_i >_+^2} \tag{40}$$

where $< \epsilon_i >_+$ are the positive principal strains. The geometrical, material and numerical parameters are given in Table 2.

Type	Parameters		Value	Unit
Geometry	Height	h	20	cm
	Depth	a	10	cm
	Notch	e	9	cm
	Width	p	5	cm
Elastic parameters	Young Modulus	E	30	GPa
	Poisson coefficient	ν	0.22	-
Damage law	Initial strain	κ_i	0.03	‰
	Failure strain	κ_c	0.2	‰
Second gradient law	Elastic modulus	B	30	kN
Penalisation	Penalty coefficient	C	10	GPa

Table 2: Mode I crack propagation test : Geometrical, material and numerical parameters

The 2D second gradient finite element [18] introduced in the finite element code Lagamine (University of Liège) by [59] has been used for the spatial discretisation. The element has 9 nodes, the displacement field is interpolated by quadratic functions of the Serendipity type, the microgradient field by linear functions and the uniform Lagrange multiplier is calculated at the central node (see also Figure 15). Following the remarks in section 2.3, the Lagrange multiplier field $\underline{\underline{\lambda}}$ is combined with a penalty coefficient C to impose the second gradient kinematics in a weak form. The numerical integration is performed using a classical Gauss scheme, [59].

The damage distribution for an imposed displacement of $20\mu m$ is given in Figure 7. A "conical" damage distribution is observed behind the fracture front.

The damage distribution (figures with blue background) and the integration points where damage is increasing (figures with grey background) around the notch tip are shown in Figure 8, for different levels of loading.

Figure 9 shows the damage distribution after a $20\mu m$-displacement. The problem is essentially one dimensional (the equivalent strain ϵ_{eq} is close or equal to ϵ_{22}) and can thus be compared to the $1D$ problem treated in section 3.1. Figure 10 gives the distribution of ϵ_{eq} and $\mathbb{D}$ for an imposed displacement of $U = 20\mu m$, along cross sections normal to the crack propagation direction x_1.

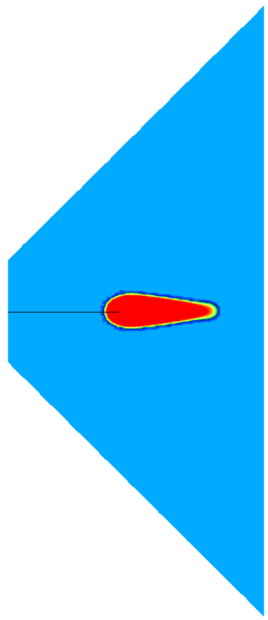

Figure 7: Mode I crack propagation test : Damage distribution for $U = 20\ \mu m$

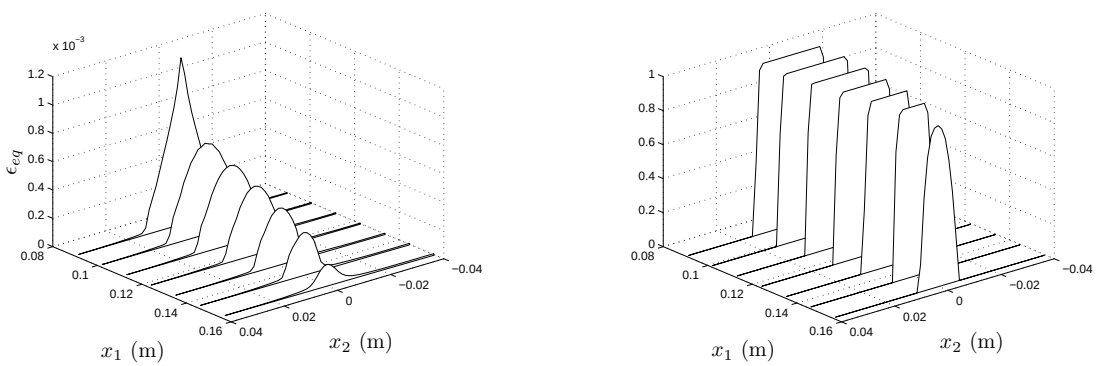

Figure 10: Distribution of ϵ_{eq} and $\mathbb{D}$ in front of the notch for $U = 20\mu m$

From Figures 7, 8, 9 and 10, it is obvious that the localization width does not stay constant but increases behind the crack front, despite the use of a constant moduli ratio between the first and the second gradient constitutive laws [22]. More specifically and as in section 3.1, the localization width stays constant where damage is below 1 (see figure 8(a)). On the cross sections where $\mathbb{D}$ reached its maximum value, the width starts to increase with increasing loading (see Figure 8(f) and Figure 10), which gives the "conical" shape damage distribution behind the fracture front.

Figure 11 gives the damage distribution along the crack propagation axis x_1 (see figure 9) for different levels of loading. On the contrary to other regularization models [30] [31], the initial damage occurs right at the notch tip ($e = 9cm$, point P on the figure). Then, damage spreads both in front of and behind the notch tip. The "process-zone" where damage varies from 0 to 1 is not of constant length and seems to be influenced by the

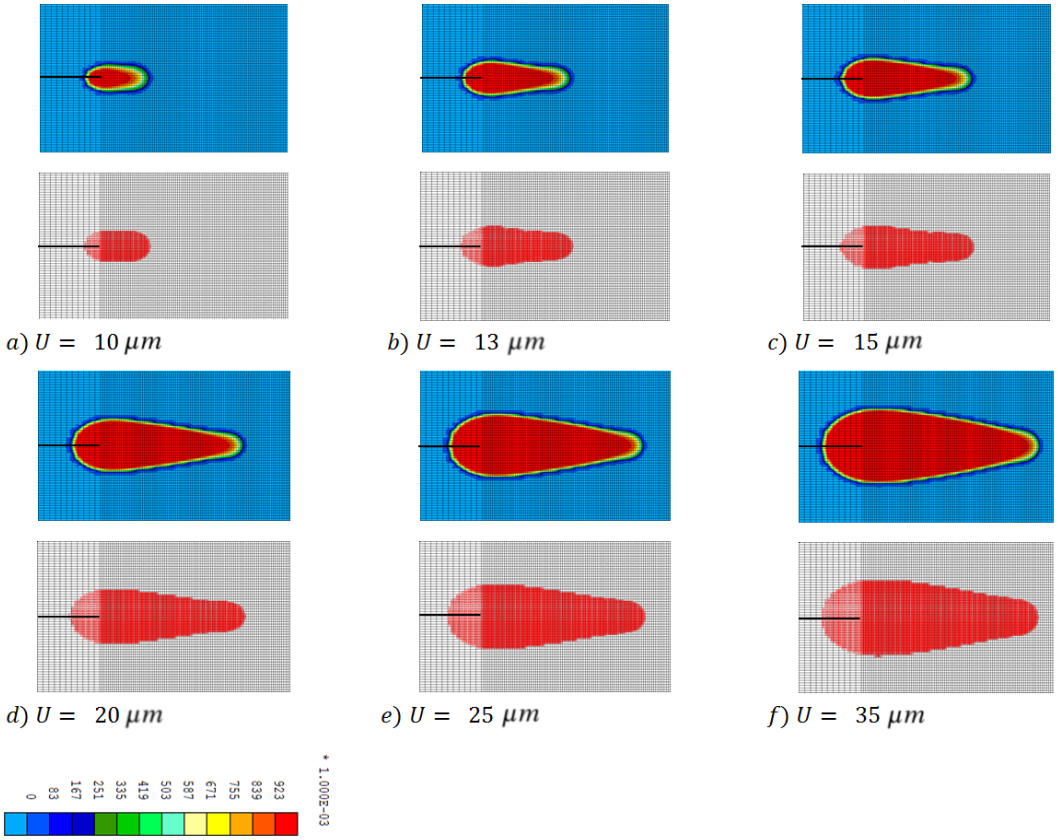

Figure 8: Damage distribution and loading integration points for different levels of loading

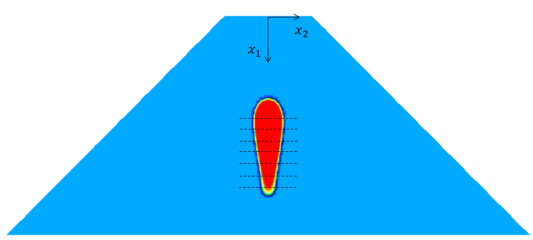

Figure 9: Damage distribution for $U = 20\ \mu m$

distance from the boundaries.

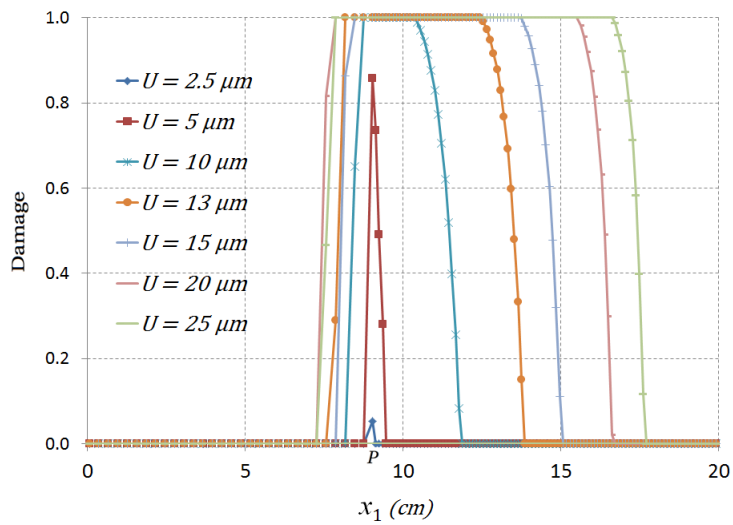

Figure 11: Damage distribution along the notch axis

The force-displacement curve (the force being equal to the reaction where the displacement U is imposed) is given in figure 12. The residual force remains important even though damage has spread throughout the specimen. As in the $1D$ test (section 3.1), this spurious residual force is due to the second gradient part, which still transmits forces despite damage values close to 1 in the localization band.

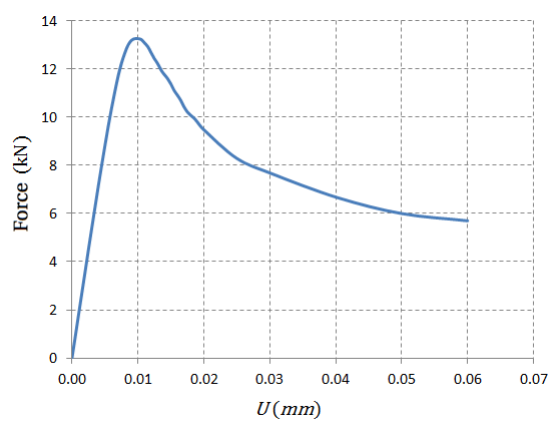

Figure 12: Force - displacement curve

Finally, another way to represent the phenomenon is the distribution of double stress components Σ_{ijk} along the axis x_2, orthogonal to the crack path (axis x_1) at a distance 0.12 m from the notch tip (Figure 13). It can be observed that the distributions of Σ_{121}, Σ_{112}, Σ_{212} and Σ_{222} change sign at the center of the localization band while Σ_{111}, Σ_{221} and Σ_{222} reach an extremum.

For an external boundary with a normal $\underline{n} = \underline{e}_2$, the tractions $\underline{s}$ and double forces $\underline{\underline{T}}$ are given according Eqs 4-5:

$$s_1 = \sigma_{12} - \frac{\partial \Sigma_{122}}{\partial x_2} - \frac{\partial \Sigma_{121}}{\partial x_1} - \frac{\partial \Sigma_{112}}{\partial x_1} \tag{41a}$$

$$s_2 = \sigma_{22} - \frac{\partial \Sigma_{222}}{\partial x_2} - \frac{\partial \Sigma_{221}}{\partial x_1} - \frac{\partial \Sigma_{212}}{\partial x_1} \tag{41b}$$

$$T_1 = \Sigma_{122} \tag{42a}$$

$$T_2 = \Sigma_{222} \tag{42b}$$

$$\tag{42c}$$

Along the crack axis, all the derivatives with respect to x_1 vanishes as the problem is essentially one-dimensional. Moreover, one observes that Σ_{222} is null along the crack axis and thus $T_2 = 0$. Its derivative however contributes to the traction component s_2. It means that tractions are still transmitted, even when σ_{22} reaches 0 for $\mathbb{D} = 1$.

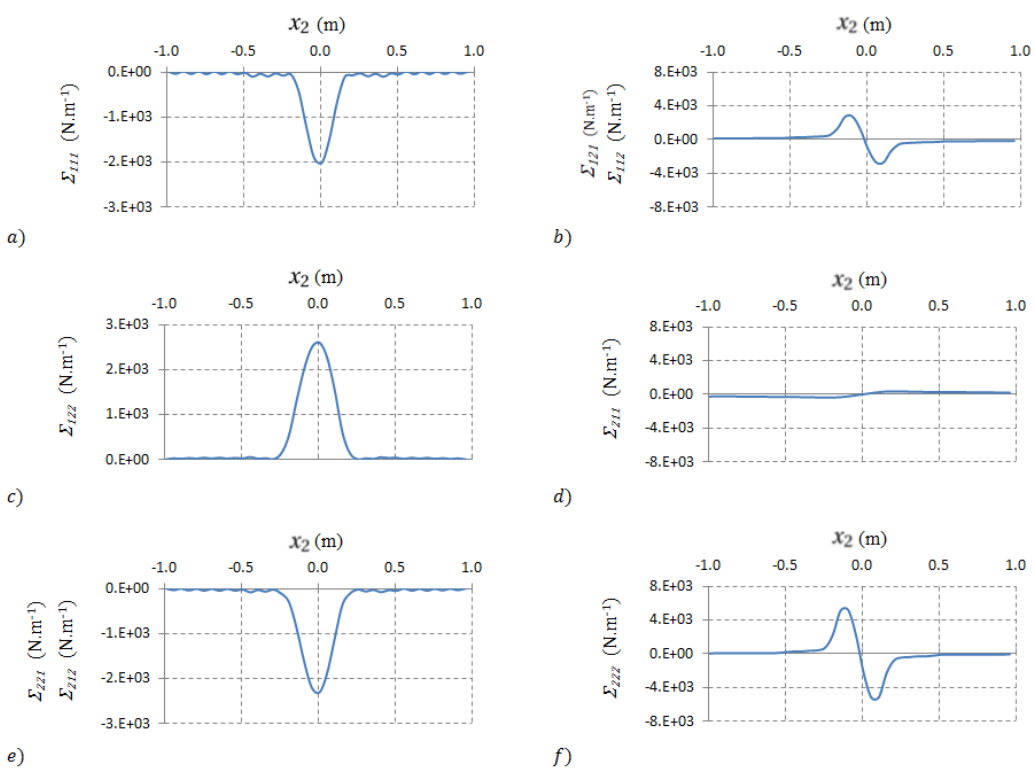

Figure 13: Mode I crack propagation test : Double stress distribution

4. A second gradient cohesive element

The previous analysis on the performance of the second gradient model as a method to numerically reproduce strain localization highlighted some deficiencies, especially for mode I crack problems. A possible solution is to

deal with the transition from a continuous medium to a discontinuous description of a crack, see for example [3] [37] [38] [4] [5] [39] [40].

Among the different approaches to perform the transition from a continuous to a discontinuous description, several authors propose the insertion of a fully formed crack (displacement discontinuity and no forces transmitted across the crack faces) when damage reaches, or is very close to 1. Such approach has been applied to resolve damage spreading in implicit gradient models [40]. Another way is to introduce the discontinuity not as a fully formed crack but as a cohesive zone, which can still transmit forces (see [3] [37]). This enables to start the transition before damage reaches 1, as some energy is dissipated in the cohesive zone.

This last choice is made hereafter as it enables taking advantage of the two approaches: the continuous damage model in a second gradient medium deals with the transition from diffuse damage to localization and predicts the path and orientation of the shear bands, while the second gradient cohesive element realistically reproduces failure. The formulation and numerical implementation of a novel second gradient cohesive element is detailed in the following.

4.1. The second gradient cohesive zone

4.1.1. Virtual work principle I - second gradient formalism

Consider a solid domain Ω with traction and double forces imposed on the boundary Γ_d and a cohesive zone with faces Γ^+_{coh} and Γ^-_{coh} (figure 14). The weak formulation takes the following form (assuming as mentioned earlier smooth boundaries):

$$\int_\Omega \underline{\underline{\sigma}} : \nabla \underline{u}^* + \overline{\Sigma} \therefore \nabla^2 \underline{u}^* d\Omega = \int_{\Gamma^+_{coh}} \underline{s}^+ . \underline{u}^* + \underline{T}^+ . D\underline{u}^* d\Gamma + \int_{\Gamma^-_{coh}} \underline{s}^- . \underline{u}^* + \underline{T}^- . D\underline{u}^* d\Gamma + \int_{\Gamma_d} \underline{s}_d . \underline{u}^* + \underline{T}_d . D\underline{u}^* d\Gamma \tag{43}$$

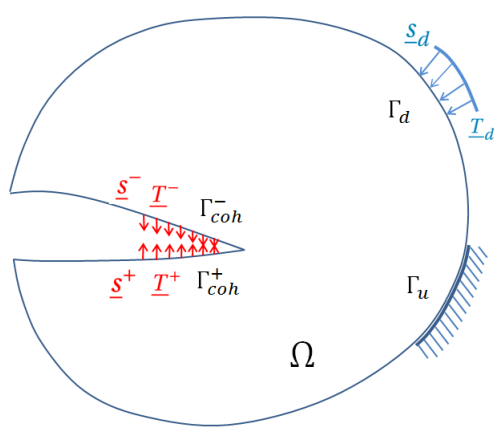

Figure 14: Solid domain with cohesive crack

where $\underline{s}^+$, $\underline{T}^+$, $\underline{s}^-$ and $\underline{T}^-$ are respectively the cohesive traction for the first gradient part and double forces for second gradient part on the faces Γ^+_{coh} and Γ^-_{coh}. $\underline{s}_d$ and $\underline{T}_d$ are the traction and the double force imposed on Γ_d.

The specific contribution of the cohesive zone part in the internal work is written as:

$$\mathcal{W}^i_{sg} = -\int_{\Gamma^+_{coh}} \underline{s}^+.\underline{u}^* + \underline{T}^+.D\underline{u}^* d\Gamma - \int_{\Gamma^-_{coh}} \underline{s}^-.\underline{u}^* + \underline{T}^-.D\underline{u}^* d\Gamma \tag{44}$$

4.1.2. Virtual work principle II - micromorphic formalism

The continuum Ω is discretized with the mixed formulation described in section 2.3 as well as for the interface element. We then have for the contribution of the cohesive zone:

$$\begin{aligned}\mathcal{W}^i_{mc} = &-\int_{\Gamma^+_{coh}} \underline{s}^+.\ \underline{u}^* + \underline{P}^+_n.\underline{v}^*_n + \underline{\underline{P}}^+_t : \left(\underline{\underline{v}}^*_t - \nabla_t \underline{u}^*\right) d\Gamma \\ &-\int_{\Gamma^-_{coh}} \underline{s}^-.\ \underline{u}^* + \underline{P}^-_n.\underline{v}^*_n + \underline{\underline{P}}^-_t : \left(\underline{\underline{v}}^*_t - \nabla_t \underline{u}^*\right) d\Gamma\end{aligned} \tag{45}$$

where the third terms in the integrals over Γ^+_{coh} and Γ^-_{coh} appear as a result of the redefinition of the surface traction in the general mixed formulation. The upper index ^{i} in equations (44) and (45) indicates that they refer to the cohesive interface part only.

4.1.3. Finite element implementation

Different choices are possible regarding the numerical implementation of a cohesive zone in a finite element model. When the crack path is known in advance, interface cohesive elements can be inserted a priori in the mesh [60] [9] [10] [61]. When the path is unknown beforehand, interface cohesive elements can be introduced during crack propagation using remeshing techniques [62] [63]. Better suited for this type of problem, X-FEM [64] [11] and embedded discontinuities [65] [66] can naturally deal with a propagating discontinuity on an unknown path.

The choice hereafter is to work with cohesive interface elements inserted a priori in the mesh (problems with known crack paths), the goal being to focus on the transition from localized strains to cracks in a second gradient medium. The second gradient cohesive element presented hereafter can however be easily extended to more general methods. The main difficulty with interface cohesive elements inserted a priori is to treat properly the initial "adherence phase", before the activation of the cohesive zone, when displacements must be continuous across the interface.

As in section 2.3, the third terms in the two integrals of equation (45) vanish when the equality $(\underline{\underline{v}}^*_t - \nabla_t \underline{u}^*)$ is correctly enforced. This equality can be weakly imposed with Lagrange multipliers :

$$\mathcal{W}^i = -\int_{\Gamma^+_{coh}} \underline{s}^+ . \underline{u}^* + \underline{P}^+_n . \underline{v}^*_n + \underline{\underline{\rho}}^+ : \left(\underline{\underline{v}}^*_t - \nabla_t \underline{u}^*\right) d\Gamma$$
$$- \int_{\Gamma^-_{coh}} \underline{s}^- . \underline{u}^* + \underline{P}^-_n . \underline{v}^*_n + \underline{\underline{\rho}}^- : \left(\underline{\underline{v}}^*_t - \nabla_t \underline{u}^*\right) d\Gamma \tag{46}$$

$$- \int_{\Gamma^+_{coh}} \underline{\underline{\rho}}^{+*} : \left(\underline{\underline{v}}_t - \nabla_t \underline{u}\right) d\Gamma - \int_{\Gamma^-_{coh}} \underline{\underline{\rho}}^{-*} : \left(\underline{\underline{v}}_t - \nabla_t \underline{u}\right) d\Gamma = 0 \tag{47}$$

with $\underline{\underline{\rho}}^+$ and $\underline{\underline{\rho}}^-$ the Lagrange multipliers field for the kinematical constraint on the faces Γ^+_{coh} and Γ^-_{coh}. In the following, it is assumed that this constraint is correctly enforced by the adjacent solid elements and therefore these terms are neglected. The validity of this assumption depends on the degree of interpolation of the Lagrange multipliers $\underline{\underline{\lambda}}$ over the domain. We thus finally have for the mixed formulation of the cohesive zone :

$$\mathcal{W}^i = -\int_{\Gamma^+_{coh}} \underline{s}^+ . \underline{u}^* + \underline{P}^+_n . \underline{v}^*_n \, d\Gamma - \int_{\Gamma^-_{coh}} \underline{s}^- . \underline{u}^* + \underline{P}^-_n . \underline{v}^*_n \, d\Gamma \tag{48}$$

As already mentioned in section 3.2, the 2D second gradient finite element [18], [59] has 9 nodes, the displacement field u_i is interpolated by biquadratic functions of the Serendipity type and the gradient field v_{ij} by bilinear functions, (Figure 15). It is thus natural to use a quadratic interpolation for $\underline{u}$ and linear interpolation for $\underline{\underline{v}}$ for the 3-noded second gradient cohesive element using the parent element coordinates ξ, as illustrated in Figure 16.

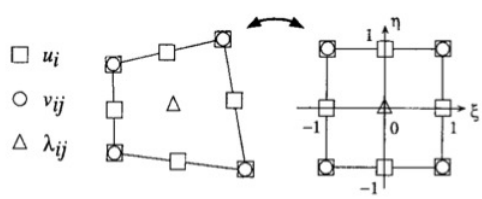

Figure 15: 2D second gradient finite element, [18], [59].

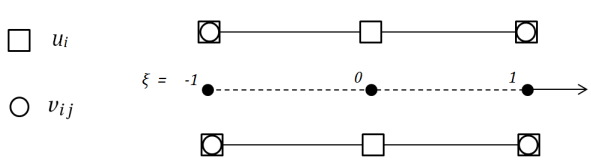

Figure 16: Second gradient cohesive interface element (parent element)

The degrees of freedom of the 3-noded second gradient cohesive interface element are (denoted with a hat $\hat{\bullet}$) :

$$\{\underline{\hat{u}}\}^T = \{\hat{u}_1|_{\xi=-1} \quad \hat{u}_2|_{\xi=-1} \quad \hat{u}_1|_{\xi=0} \quad \hat{u}_2|_{\xi=0} \quad \hat{u}_1|_{\xi=1} \quad \hat{u}_2|_{\xi=1}\} \tag{49}$$

$$\{\underline{\hat{v}}\}^T = \{\hat{v}_{11}|_{\xi=-1} \quad \hat{v}_{12}|_{\xi=-1} \quad \hat{v}_{21}|_{\xi=-1} \quad \hat{v}_{22}|_{\xi=-1} \quad \hat{v}_{11}|_{\xi=1} \quad \hat{v}_{12}|_{\xi=1} \quad \hat{v}_{21}|_{\xi=1} \quad \hat{v}_{22}|_{\xi=1}\} \tag{50}$$

As usual, the displacement field has the form of a column vector (notated $\{\bullet\}$) and is expressed as a product of the interpolation functions matrix with the nodal degrees of freedom. For the faces Γ^+_{coh} and Γ^-_{coh} we have:

$$\{\underline{u}^+\} = [N_u]\,\{\underline{\hat{u}}^+\} \tag{51a}$$

$$\{\underline{u}^-\} = [N_u]\,\{\underline{\hat{u}}^-\} \tag{51b}$$

and on $\partial\Omega$

$$\{\underline{v}\} = [N_v]\,\{\underline{\hat{v}}\} \tag{52}$$

According to equation (A.5), on the boundary, $\underline{v}_n = \underline{\underline{v}}.\underline{n}$, that reads in index notation:

$$\underline{v}_{ni} = v_{ij} n_j$$

Consequently, it can be checked that the FE discretization of $\underline{v}_n$ on $\partial\Omega$ reads:

$$\{\underline{v}_{\ n}\} = [N_{vn}]\,\{\underline{\hat{v}}\}$$

where the 2x8 matrix $[N_{vn}]$ reads:

$$[N_{vn}] = \begin{pmatrix} n_1 & n_2 & 0 & 0 \\ 0 & 0 & n_1 & n_2 \end{pmatrix} [N_v]$$

n_1 and n_2 being the component of the normal vector determined on the edge of the element between two nodes situated on $\partial\Omega$. For the faces Γ^+_{coh} and Γ^-_{coh} that reads:

$$\left\{\underline{v}_{\ n}^{\ +}\right\} = \left[N^+_{vn}\right]\,\{\underline{\hat{v}}^+\} \tag{53a}$$

$$\left\{\underline{v}_{\ n}^{\ -}\right\} = \left[N^-_{vn}\right]\,\{\underline{\hat{v}}^-\} \tag{53b}$$

where the n_1 and n_2 are the components of the vector $\{e_n\}$ defined below.

The geometric discretization is of isoparametric type :

$$\{x^+\} = [N_u]\,\{\hat{x}^+\} \tag{54a}$$

$$\{x^-\} = [N_u]\,\{\hat{x}^-\} \tag{54b}$$

To express the cohesive law in terms of normal and tangential traction, a local coordinate system is defined as a function of the mean coordinates :

$$\{e_t\} = \frac{1}{|\underline{J_m}|}\begin{Bmatrix} \frac{\partial x_1^m}{\partial \xi} \\ \frac{\partial x_2^m}{\partial \xi} \end{Bmatrix} \qquad \{e_n\} = \frac{1}{|\underline{J_m}|}\begin{Bmatrix} -\frac{\partial x_2^m}{\partial \xi} \\ \frac{\partial x_1^m}{\partial \xi} \end{Bmatrix} \tag{55}$$

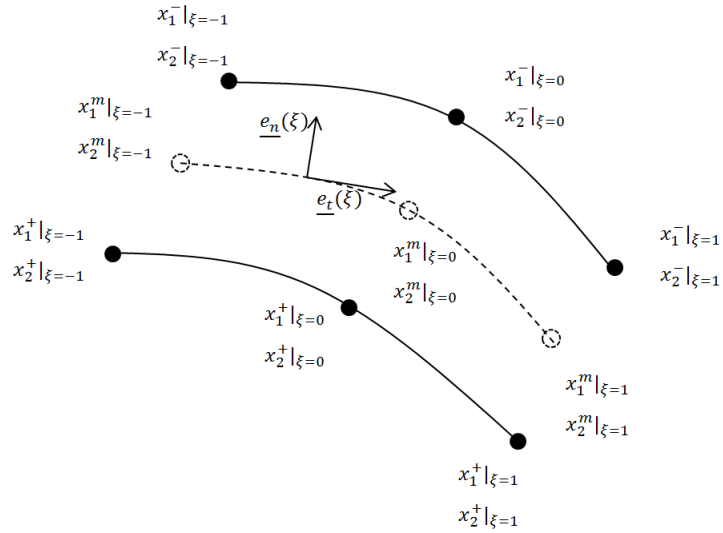

Figure 17: Geometrical interpolation and local coordinate system

with :

$$\{x^m\} = \frac{1}{2}\left(\{x^-\} + \{x^+\}\right) \tag{56}$$

$$|J_m| = \sqrt{\left(\frac{\partial x_1^m}{\partial \xi}\right)^2 + \left(\frac{\partial x_2^m}{\partial \xi}\right)^2} \tag{57}$$

The matrix for the coordinate change is denoted as $[R]$:

$$[R] = \frac{1}{|\underline{J_m}|}\begin{bmatrix} \frac{\partial x_1^m}{\partial \xi} & -\frac{\partial x_2^m}{\partial \xi} \\ \frac{\partial x_2^m}{\partial \xi} & \frac{\partial x_1^m}{\partial \xi} \end{bmatrix} \tag{58}$$

The cohesive tractions $\underline{s}^+$, $\underline{s}^-$, $\underline{T}^+ = \underline{P}_n^+$, $\underline{T}^- = \underline{P}_n^-$ are written in this local coordinate system :

$$\underline{s} = \underline{s}^+ = -\underline{s}^- = \begin{Bmatrix} s_n \\ s_t \end{Bmatrix} \tag{59}$$

$$\underline{T} = \underline{T}^+ = -\underline{T}^- = \begin{Bmatrix} T_n \\ T_t \end{Bmatrix} \tag{60}$$

Using expression (51) and (52) for the discretization of the fields $\underline{u}$ and $\underline{v}$ over the faces Γ_{coh}^+ and Γ_{coh}^- and the expression of the cohesive traction in the local coordinate system (59) and (60), the discretized weak formulation for the cohesive interface element is given by (the integrals are considered over the deformed configuration):

$$
\begin{aligned}
\mathcal{W}^i = & -\int_{\Gamma^+_{coh}} \{\hat{\underline{u}}^{*+}\}^T [N_u]^T [R]^T \{\underline{s}\} d\Gamma - \int_{\Gamma^+_{coh}} \{\hat{\underline{v}}^{*+}\}^T \left[N^+_{nv}\right]^T [R]^T \{\underline{T}\} d\Gamma \\
& + \int_{\Gamma^-_{coh}} \{\hat{\underline{u}}^{*-}\}^T [N_u]^T [R]^T \{\underline{s}\} d\Gamma + \int_{\Gamma^-_{coh}} \{\hat{v}^{*-}\}^T \left[N^-_{nv}\right]^T [R]^T \{\underline{T}\} d\Gamma \\
= & -\int_{-1}^{1} \{\hat{\underline{u}}^{*+}\}^T [N_u]^T [R]^T \{\underline{s}\} |J^+| d\xi - \int_{-1}^{1} \{\hat{\underline{v}}^{*+}\}^T \left[N^+_{nv}\right]^T [R]^T \{\underline{T}\} |J^+| d\xi \\
& + \int_{-1}^{1} \{\hat{\underline{u}}^{*-}\}^T [N_u]^T [R]^T \{\underline{s}\} |J^-| d\xi + \int_{-1}^{1} \{\hat{\underline{v}}^{*-}\}^T \left[N^-_{nv}\right]^T [R]^T \{\underline{T}\} |J^-| d\xi
\end{aligned}
\tag{61}
$$

where we used :

$$
|J^+| = \sqrt{\left(\frac{\partial x_1^+}{\partial \xi}\right)^2 + \left(\frac{\partial x_2^+}{\partial \xi}\right)^2} \tag{62}
$$

.

$$
|J^-| = \sqrt{\left(\frac{\partial x_1^-}{\partial \xi}\right)^2 + \left(\frac{\partial x_2^-}{\partial \xi}\right)^2} \tag{63}
$$

4.2. From localised strains to cohesive zones and to fully opened cracks

It has been illustrated in the literature that the second gradient model [14] [15] [16] [17] [18] regularizes strain localisation problems and provides results that are mesh independent (see among others [19] [20] [2] [21] [22] [23] [24]). Nevertheless, in section 3 it is shown that the second gradient model does not deal with the transition from localised strains to cracks, resulting sometimes to spurious resistant forces due to the non vanishing second gradient terms. The second gradient cohesive element proposed in this article bypasses this limitation by reproducing correctly the transition from localised strains to a cohesive zone and finally to a fully opened crack.

A similar approach but on a classical medium and for damage models has been presented in [3] [37] and [5]. In [37] and [5] for example, the activation criteria for the cohesive element is a critical damage value (not necessarily close to 1). Furthermore, an equivalence between the continuous damage model and the cohesive zone has to be provided in order to determine the shape and parameters of the cohesive law. In [3], the (locally) dissipated energy is chosen to be the same as the completely continuous solution (without transition to a cohesive zone). These points are studied hereafter but for a second gradient medium.

In the proposed methodology, the second gradient interface element is a priori inserted in the mesh, before any crack propagation. Special care should be therefore given to deal with this phase, prior to the second gradient interface element activation, where the interface element should only enforce the continuity of the displacement and displacement gradient fields across its (closed) faces (Adherence phase). Once the transition criterion reached (detailed in section 4.2.2), the cohesive law is activated and the crack propagates (Activation - transition phase).

A jump (denoted hereafter with a double bracket) is computed as the difference of the kinematic quantities between the two faces of the interface element :

$$[\![\underline{u}]\!] = \underline{u}^- - \underline{u}^+ \tag{64}$$

$$[\![\underline{v}_n]\!] = \underline{v}_n^- - \underline{v}_n^+ \tag{65}$$

The cohesive element (Figure 18) is activated once damage (in the element) reaches a critical value $\mathbb{D}_{cr}$. The condition requires the evaluation of the damage variable $\mathbb{D}$, function of the strain tensor $\underline{\underline{\epsilon}}$. In the cohesive element however, the derivative of $\underline{u}$ is not known in the normal direction (the displacement is interpolated only in the tangential direction). The strain tensor in equation 19 is therefore calculated using $\underline{\underline{v}}$ instead. A similar proposal was made in [21] as it helps avoiding spurious oscillations due to the weak formulation of the kinematic constraint when using a constant Lagrange multiplier field per element. Other possible solutions could be either to interpolate the damage field [37] or to increase the interface element connectivity by including nodes belonging to the neighboring solid elements.

Finally, it is assumed that no damage evolution occurs around the cohesive crack after the activation.

4.2.1. Adherence phase ($\mathbb{D} < \mathbb{D}_{cr}$)

Continuity of the displacement and gradient fields across the second gradient cohesive element interface implies that no jumps appear (they are equal to 0). It should be noted that if $[\![\underline{u}]\!] = 0$ and $\underline{\underline{v}}_t = \nabla_t \underline{u}$ is correctly enforced, the continuity on the tangential part of $\underline{\underline{v}}$ is automatically met ($[\![\underline{\underline{v}}_t]\!] = 0$). Only the continuity on the normal part should be therefore imposed $[\![\underline{\underline{v}}_n]\!] = 0$. One simple way to impose $[\![\underline{u}]\!] = 0$ and $[\![\underline{\underline{v}}_n]\!] = 0$ is the use of penalty method, replacing in equation (48), (see also equation (16)):

$$\underline{s} = \underline{s}^+ = -\underline{s}^- = C_u [\![\underline{u}]\!] \tag{66}$$

$$\underline{T} = \underline{T}^+ = -\underline{T}^- = C_h [\![\underline{v}_n]\!] \tag{67}$$

with C_u and C_h the penalty coefficients on the displacement and displacement gradient jumps. Compared to the use of Lagrange multipliers, the penalty method offers the advantage of not introducing additional degree of freedom. Nevertheless, choosing the appropriate penalty coefficient is not straightforward, particularly in this case, as two penalty coefficients have to be adopted for two non independent fields. In practice, a trial and error procedure is required in order to find a set of two constants which sufficiently enforce the continuity with adequate convergence rate of the Newton-Raphson procedure. More specifically, the procedure consists in increasing them progressively till ensuring the continuity through the cohesive element. Too high values of the penalty coefficients should be avoided, as the convergence of the Newton-Raphson scheme can be jeopardized. Consequently, between two sets of penalty coefficients assuring continuity, the one with the smaller values is chosen.

4.2.2. Activation and transition parameters ($\mathbb{D} >= \mathbb{D}_{cr}$)

Once the critical damage value reached, the cohesive zone is activated to model the progressive "debonding" of the two faces. The evolution of the traction stress $\underline{s}$ and normal double stress $\underline{P}_n$ are defined hereafter.

First gradient part. Mode I crack propagation is considered, i.e. the local behavior around the crack is supposed one-dimensional; the normal part of the cohesive traction is function only of the displacement jump in the normal direction $[\![u_n]\!]$ (simply denoted $[\![u]\!]$ hereafter), the tangential part is supposed null. The cohesive zone is activated at any point where damage is greater than a specified value $\mathbb{D}_{cr}$ and $s_n(\mathbb{D}_{cr})$ is the corresponding cohesive traction (the normal component of the first gradient part of the cohesive traction at the activation time). A linear cohesive law (figure 18) is adopted, that can be defined by the critical displacement jump $[\![u_c]\!]$ (beyond which traction stresses vanish) or the energy dissipated by the cohesive law G_c. In the following, the critical displacement jump is used. The evolution of the traction stress is given by:

If $[\![u]\!] < [\![u_c]\!]$:

$$s_n = \frac{s_n(\mathbb{D}_{cr})}{s_n(\mathbb{D}_{cr})/C_u - [\![u_c]\!]}([\![u]\!] - [\![u_c]\!]) \tag{68}$$

If $[\![u]\!] >= [\![u_c]\!]$:

$$s_n = 0 \tag{69}$$

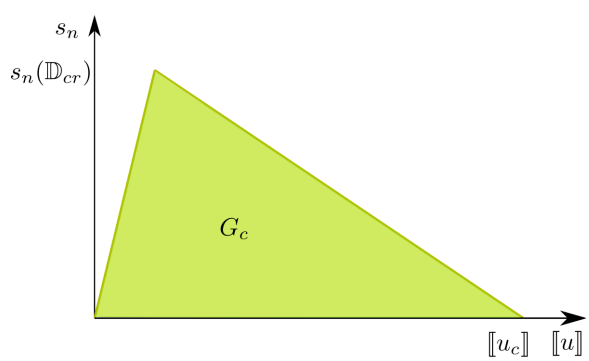

Figure 18: First gradient cohesive law

The total energy dissipated for the creation of a unit crack is the sum of the energy dissipated by the damage law $G_{\mathbb{D}}$ and the energy dissipated by the cohesive law G_c. For the damage part, the calculation of the dissipated energy for the one-dimensional case and for a constant localization length l_s was given in section 3.1.2 :

$$G_{\mathbb{D}} = \int_L \int_0^{\mathbb{D}(x)} Y d\mathbb{D} dx = \int_{l_s} \int_0^{\mathbb{D}} Y d\mathbb{D} dx \tag{70}$$

The energy dissipated in the cohesive zone is simply :

$$G_c = \int_0^{[\![u_c]\!]} s \; d[\![u_c]\!] \tag{71}$$

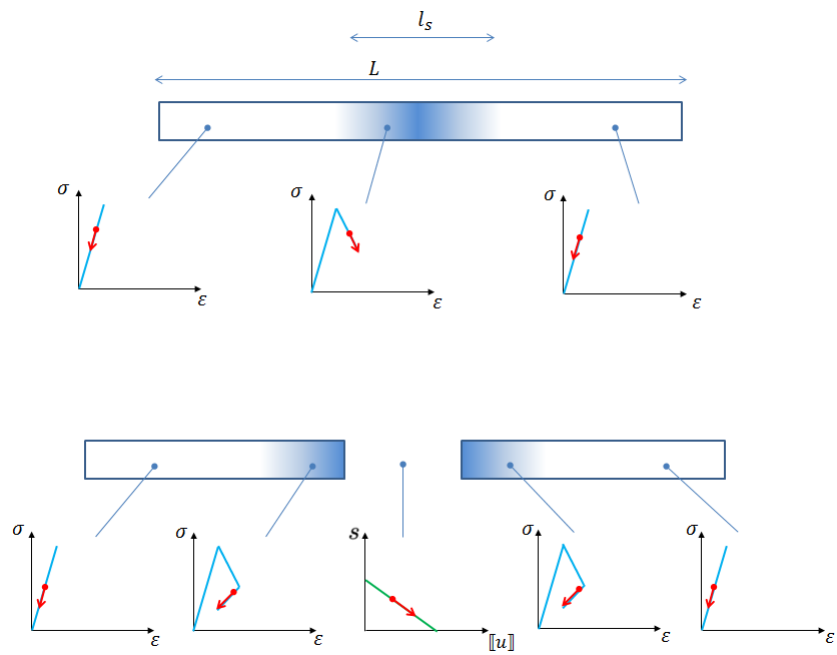

Figure 19: Continuous - discontinuous transition in the 1D case

The total dissipated energy is finally:

$$G = G_{\mathbb{D}} + G_c \tag{72}$$

It is assumed that damage does not evolve around the cohesive crack after the activation and the corresponding element unloads elastically (see Figure 19). In practice, it might be necessary to fix the damage evolution in the localization zone once the cohesive law activated [37], see also Figure 22. If the local behavior is close to a one-dimensional problem, equation (70) and (71) can be used to estimate the dissipated energy for a unit crack and to choose the appropriate set of cohesive law parameters.

Second gradient part. For the one-dimensional traction case of section 3.1, no double force exists at activation corresponding to maximum damage and maximum strain. At this point the second derivative of the displacement is null and therefore according the second gradient elastic constitutive law, the double stress vanishes. Once the cohesive zone activated, its traction must be in equilibrium with the stresses in the solid. The double stress being zero, the corresponding double traction $\underline{T}$ of the cohesive law should be also null.

In the 2D mode I crack propagation case however, tangential double force may exist for a surface with a normal orthogonal to crack path, as shown in Figure 13. The double traction $\underline{T}$ must then be accounted by the cohesive law. It is chosen hereafter to use an additional linear cohesive law linking $\underline{T}$ with $[\![u]\!]$ with the same final displacement jump $[\![u_c]\!]$ as for the first gradient part ($\underline{T}(\mathbb{D}_{cr})$ being the second gradient part of the cohesive traction at activation time).

If $[\![u]\!] < [\![u_c]\!]$:

$$\underline{T} = \frac{\underline{T}(\mathbb{D}_{cr})}{s_n(\mathbb{D}_{cr})/C_u - [\![u_c]\!]}([\![u]\!] - [\![u_c]\!]) \tag{73}$$

If $[\![u]\!] >= [\![u_c]\!]$:

$$\underline{T} = 0 \tag{74}$$

The choice to link the traction to the displacement jump is classical in the literature, it ensures that traction is null for the given critical displacement jump. When considering the double traction however, the natural assumption is to link it to the normal displacement gradient jump. This choice is not adopted here as it is important to ensure that traction and double traction become zero simultaneously (other choices are of course possible). One should also consider that this additional cohesive law introduces an additional dissipative term in the model.

4.2.3. Some numerical aspects

Activation of the cohesive element. Before activation, the cohesive element is very stiff and develops no damage. The behavior of the 2D finite element connected to one face of the cohesive element is initially elastic with damage developing as a function of strain. The cohesive element is activated when damage at the fracture face reaches a critical value $\mathbb{D}_{cr}$. In practice, for an incremental loading within the Newton-Raphson algorithm, activation is done when damage at the last converged step is greater than the critical damage value $\mathbb{D}_{cr}$ (see also [37] [40] and [3]). Indeed, if activation is allowed during the iterations, convergence may not occur as the displacement correction often oscillates between the adherence and the activation-transition phases.

Depending on the load increment size, the actual value of damage at the activation point $\mathbb{D}_{tr}$ can significantly differ from the specified value $\mathbb{D}_{cr}$. It is however possible to keep the dissipated energy by unit crack length constant by adjusting the cohesive law as shown in Figure 20 (see also [3] [37]).

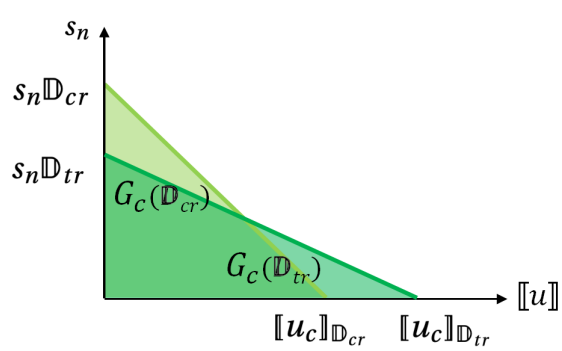

Figure 20: Adjusting the first gradient cohesive law as a function of $\mathbb{D}_{tr}$

4.3. The two-dimensional mode I crack propagation problem revisited

The mode I crack propagation problem of section 3.2 is hereafter revisited considering a second gradient medium and second gradient cohesive elements positioned a priori on the crack path (Figure 21).

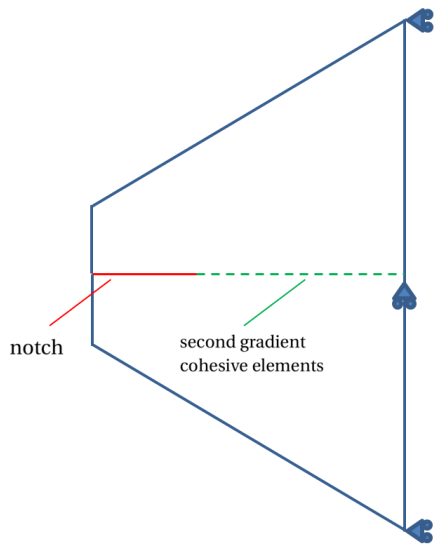

Figure 21: Mode I crack propagation test revisited : Second gradient cohesive elements

The material parameters of the second gradient medium are the ones presented in Table 2, while for the cohesive second gradient element $[\![u_c]\!] = 0.2mm$ and $\mathbb{D}_{cr} = 0.99$. The penalty coefficients for the adherence phase C_u and C_h are taken equal to 10^{16} $Pa.m^{-1}$ and 10^{15} $Pa.m$ respectively. No adjustment of the cohesive law is considered to keep the dissipated energy constant. During computation, every time the critical damage value $\mathbb{D}_{cr}$ is exceeded at the integration point of a second gradient cohesive interface element, damage is blocked on the 2D second gradient elements left and right of the interface (normal direction) on a width at least equal to the localization length. This is facilitated by using a regular mesh near the crack axis (Figure 22), [37]). It is recalled that for one-dimensional behavior the localization length is approximated by equation (27).

It is obvious in Figure 23 that the introduction of second gradient cohesive elements significantly improves the behavior. The transition to a cohesive zone allows to reduce the residual force and to correctly simulate crack opening.

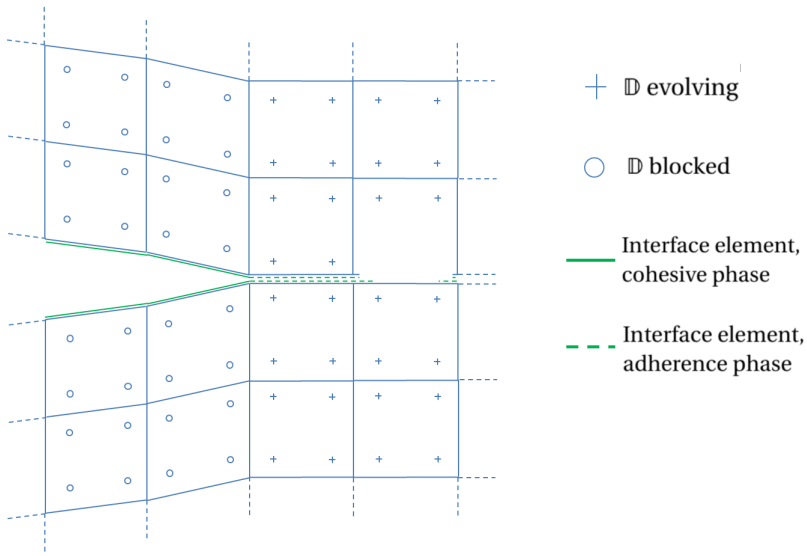

Figure 22: Fixing damage on adjacent elements during the cohesive zone propagation

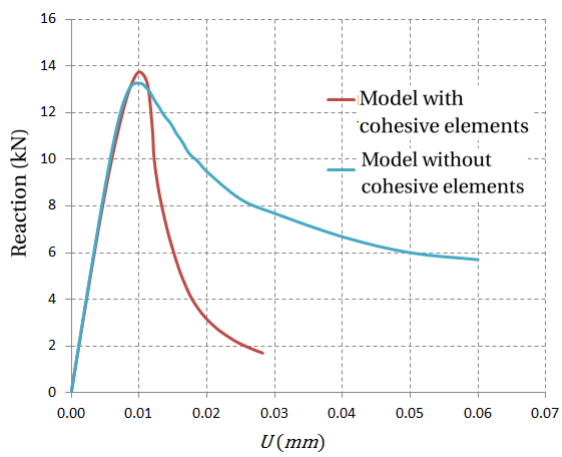

Figure 23: Mode I crack propagation test revisited: Global force - imposed displacement curve

The damage distribution for an imposed displacement of $25\mu m$ is given in Figure 24. Figure 25 shows the damage distribution as well the integration points in front of the notch where damage increases for different imposed displacements. The damage zone width in the direction orthogonal to the crack path does not remain exactly constant during the loading despite the fact that activation is done before damage reached 1. This is due to $2D$ effects, notably at the notch tip and near the boundaries. Nevertheless, when the crack tip is far from the notch tip and the boundaries, the damage process zone width remains constant (figures 25 c) and d)). At crack initiation or when the crack reaches the opposite boundary, the hypothesis of one dimensional behavior around the crack is not correct (figures 25 a), b) and e), f)).

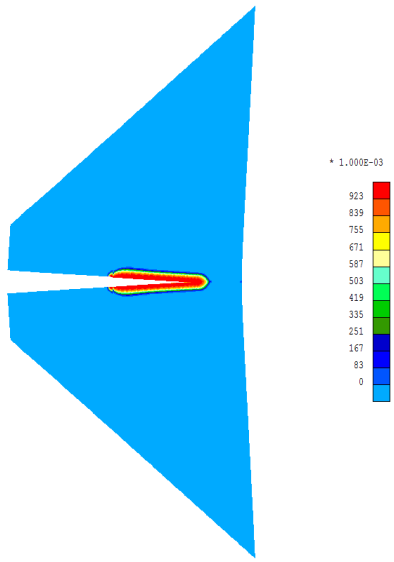

Figure 24: Mode I crack propagation test revisited : Damage distribution for $U = 25\mu m$

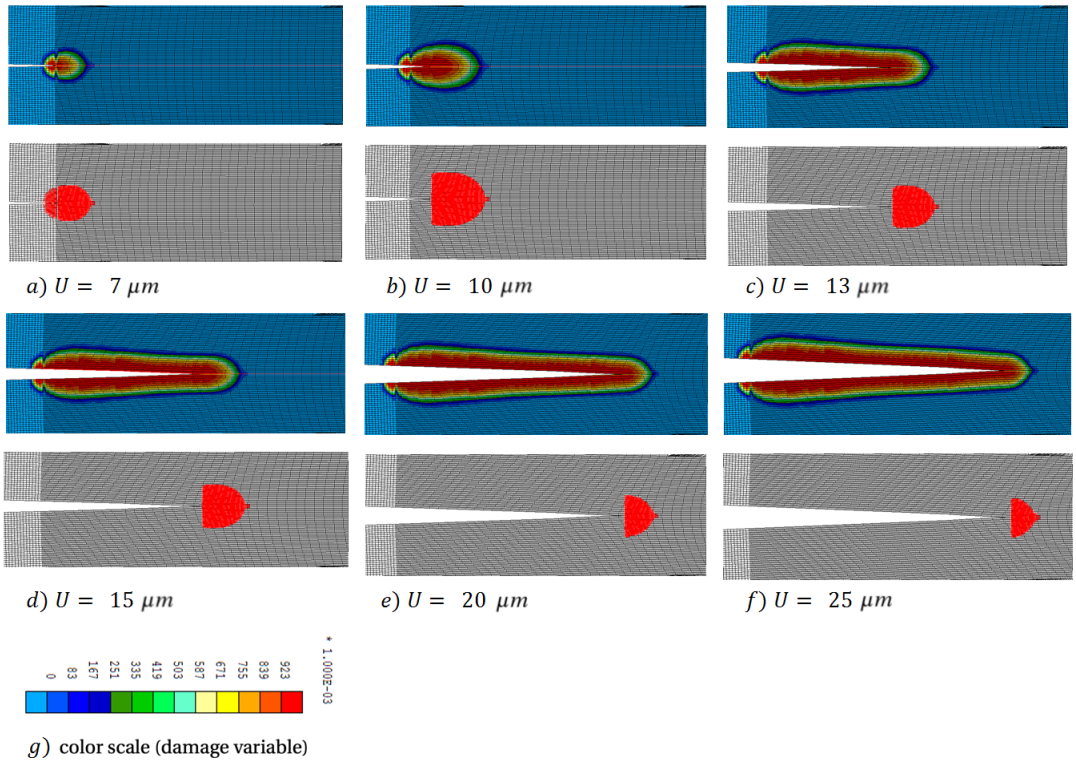

Figure 25: Mode I crack propagation test revisited: Damage distribution and loading integration points

4.4. 3 points bending test

Within the French research program ANR MEFISTO, a series of 3 points bending tests on plane concrete beams have been performed in order to study scale effects and the crack evolution [67], [68]. The specimen $D2$

of the experimental campaign is simulated hereafter. The geometry of the $D2$ concrete beam and the boundary conditions are shown in figure 26. The bending tests were performed with a controlled Notch Mouth Opening Displacement (NMOD) rate of $0.05\mu m/s$. This type of control allows obtaining a gradual increase in the crack openings and at a later stage (post-peak regime) a steady decrease of the load bearing capacity.

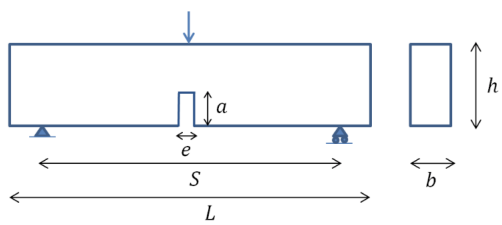

Figure 26: 3 points bending test: Geometry (see also Table3)

Second gradient finite elements [18] and the proposed cohesive second gradient element are used to discretize the beam. The finite element mesh and the position of the cohesive elements are shown in figures 27 and 28. The mesh is refined along the expected crack path in order to have a sufficient number of cohesive elements (300 along the beam height). Outside this zone, the mesh is regular in order to facilitate blocking the damage evolution on the integration points upon activation of the cohesive zone. A monotonically increasing vertical displacement is applied at the top of the beam, see figure 27. A bilinear damage constitutive law is adopted

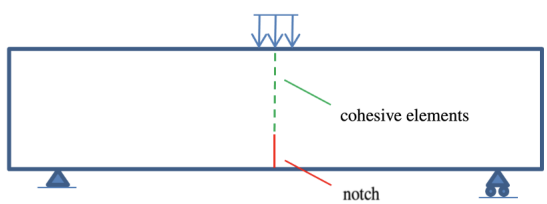

Figure 27: 3 points bending test: Position of the cohesive elements

for the 1st gradient part and an elastic law for the 2nd gradient part. The parameters of the constitutive and the cohesive laws are given in table 3. The material parameters of the 1st gradient constitutive law provide a tangent modulus of the softening part $G_{tg} = -2.8110^{10} Pa$. Using equation 27, a first estimation of the width of the localization zone can be found $\lambda \approx 1.2cm$. This width stays constant as a bilinear damage constitutive law is adopted [22] and the transition to the cohesive zone is done for $D = 0.95$.

The comparison of the experimental with the numerical results in terms of reaction forces-NMOD are given in figure 29. The damage distribution for NMOD=100 μm is provided in figure 30. It can be observed that the numerical results reproduce correctly the experimental ones up to the peak and at the beginning of the softening phase. Significant differences of the two curves appear later on, at the final loading stages. This however can be certainly improved by an enhancement of the adopted cohesive law. The width of localization

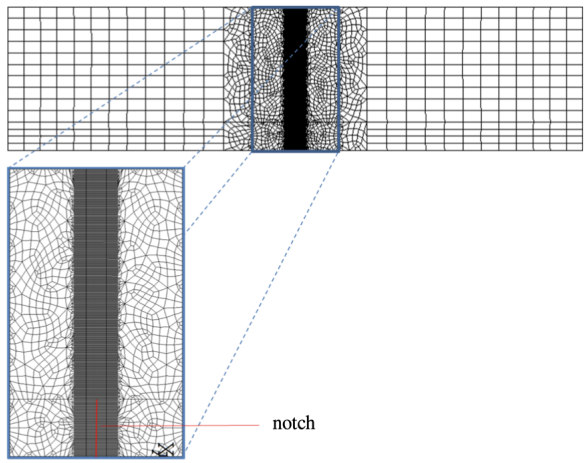

Figure 28: 3 points bending test: Finite element mesh

zone remains limited even at the final stages of the loading and the crack opening can be clearly visualized.

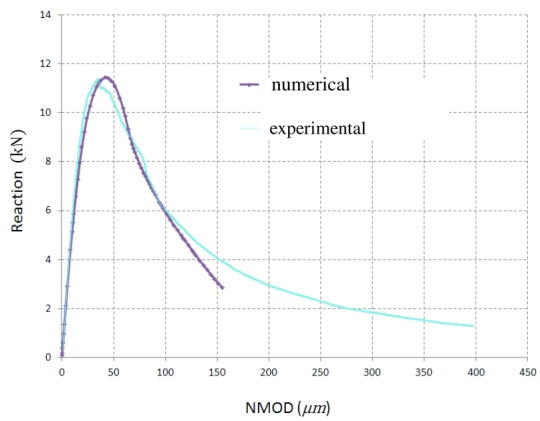

Figure 29: 3 points bending test: Reaction force - NMOD (numerical and experimental results)

Remark: The relatively fine finite element meshes used for the mode I crack propagation test and the 3 points bending test are due to the fact that one needs at least three to four finite elements inside the localisation zone to reproduce correctly the softening behavior. Thirty minutes are needed to complete the calculations.

Type	Parameters		Value	Unit
Geometry	Length	L	80	cm
	Span	S	60	cm
	Height	h	20	cm
	Depth	b	10	cm
	Notch width	e	3	mm
	Notch height	a	4	cm
Elastic parameters	Young Modulus	E	30	GPa
	Poisson coefficient	ν	0.22	-
Damage law	Initial strain	κ_i	0.03	‰
	Failure strain	κ_c	0.2	‰
Second gradient law	Elastic modulus	B	100	kN
Cohesive law	Critical damage	$\mathbb{D}_{cr}$	0.95	
	Critical displacement jump	$[\![u_c]\!]$	0.04	mm

Table 3: 3 points bending test : Geometrical, material and numerical parameters (see also figure 26)

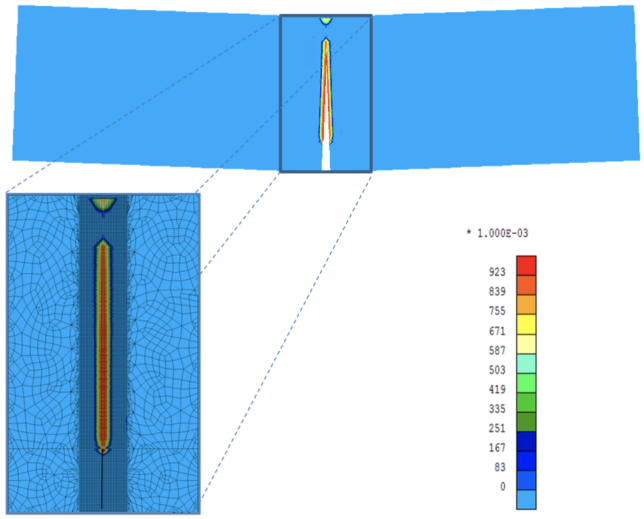

Figure 30: 3 points bending test: Damage distribution for NMOD=100 μm.

5. Conclusion

Modeling strain localization with a second gradient model can become problematic at the late stages of softening response, when the second gradient terms become significant compared to the first gradient terms. This is particularly true for mode I crack problems where a spurious spreading of the damaged zone is often encountered. A novel second gradient cohesive interface element for mode I crack propagation problems is

proposed to deal with these limitations. The combination of second gradient finite elements and second gradient cohesive interface elements permits to correctly reproduce all the different phases up to failure; the adherence phase, strain localisation, the transition from localised strains to cohesive zones and full crack opening.

In order to extend the model to more complex stress conditions (mode 2), several improvements should be engaged: adopting a more effective damage mechanics model for shear loading and introducing the shear component in the cohesive finite element formulation following a similar approach as the one prescribed in this article. Finally, in order to predict the fracture location (and not to assume it as an input), the second gradient cohesive element should be positioned between all finite element edges.

Appendix A Splitting in normal and tangential parts

The kinematics of a micromorphic continuum are described by a displacement field $\underline{u}$ and a micro strain field $\underline{\underline{v}}$. According to Germain [6] the internal virtual work of such a continuum occupying a bounded domain Ω reads:

$$\mathcal{W}^i_{mc} = \int_\Omega \left(\underline{\underline{\sigma}} : \nabla \underline{u}^* + \underline{\underline{\tau}} : \left(\underline{\underline{v}}^* - \nabla \underline{u}^* \right) + \overline{\Sigma} \therefore \nabla \underline{\underline{v}}^* \right) d\Omega \tag{A.1}$$

where $\underline{u}^*$ and $\underline{\underline{v}}^*$ denote respectively the virtual displacement and the virtual micro strain fields and $\therefore$ the scalar product of two third order tensors. Consistently with that expression of the internal virtual work, the weak formulation of the equilibrium of a micromorphic continuum, in case no external volume forces are applied, reads:

$$\int_\Omega \left(\underline{\underline{\sigma}} : \nabla \underline{u}^* + \underline{\underline{\tau}} : \left(\underline{\underline{v}}^* - \nabla \underline{u}^* \right) + \overline{\Sigma} \therefore \nabla \underline{\underline{v}}^* \right) d\Omega = \int_{\partial\Omega} \left(\underline{p}.\underline{u}^* + \underline{\underline{P}} : \underline{\underline{v}}^* \right) d\Gamma \tag{A.2}$$

which holds for any field $\underline{u}^*$ and $\underline{\underline{v}}^*$.

The previous equation introduces a number of stress tensors and contact forces : the classical stress tensor $\underline{\underline{\sigma}}$ dual of the macro strains $\nabla \underline{u}$, the so-called microstress tensor dual of the difference $\left(\underline{\underline{v}} - \nabla \underline{u} \right)$ and the so-called double stress third order tensor $\overline{\Sigma}$ dual of $\nabla \underline{\underline{v}}$ acting on the domain Ω. $\underline{p}$ and $\underline{\underline{P}}$ are respectively the force and the double force surface densities applied on the boundary $\partial\Omega$. In case of a micromorphic continuum and according to the boundary value problem considered, they can be known (totally or partially), or unknown.

Considering $\underline{\underline{v}}^* = \nabla \underline{u}^*$ in the external virtual work of the micromorphic continuum should be done carefully because $\underline{u}^*$ and $\nabla \underline{u}^*$ cannot be given independently. In the same way, for duality reason the external surface force $\underline{p}$ and double force $\underline{\underline{P}}$ densities cannot be chosen independently [15]. A way to deal with this is to split the tensors $\underline{\underline{P}}$ and $\underline{\underline{v}}^*$ into normal and tangential parts.

Let $\underline{n}$ the external normal at some (smooth) point of $\partial\Omega$ and $Q_\perp$ the normal projection onto the tangential plane. Note that in a 2D problem $Q_\perp = \underline{t} \otimes \underline{t}$ where $\underline{t}$ is the unit tangent vector to $\partial\Omega$. As the identity tensor $\mathbb{I}$ reads :

$$\mathbb{I} = \underline{n} \otimes \underline{n} + Q_\perp \tag{A.3}$$

then, through a right hand side composition, the tensor $\underline{\underline{P}}$ can be written:

$$\underline{\underline{P}} = \underline{P}_n \otimes \underline{n} + \underline{\underline{P}}_t \tag{A.4}$$

where

$$\underline{P}_n = \underline{\underline{P}}.\underline{n} \tag{A.5}$$

$$\underline{\underline{P}}_t = \underline{\underline{P}} \circ Q_\perp \tag{A.6}$$

in which the symbol "$\circ$" denotes the composition product of two linear operators. The tensor $\underline{\underline{v}}^*$ is split in a similar way into $\underline{\underline{v}}^* = \underline{v}_n^* \otimes \underline{n} + \underline{\underline{v}}_t^*$. It can be checked that $\underline{P}_n \otimes \underline{n} : \underline{\underline{v}}_t^* = \underline{\underline{P}}_t : \underline{v}_n^* \otimes \underline{n} = 0$ so, with those decompositions, the scalar product of $\underline{\underline{P}}^*$ and $\underline{\underline{v}}^*$ reads:

$$\underline{\underline{P}}^* : \underline{\underline{v}}^* = \underline{P}_n.\underline{v}_n^* + \underline{\underline{P}}_t : \underline{\underline{v}}_t^* \tag{A.7}$$

The introduction of $(\nabla \underline{u}^*)_t = \nabla_t \underline{u}^*$ in the weak formulation of the equilibrium of a micromorphic continuum [6], in case no external volume forces are applied, yields:

$$\int_{\partial\Omega} \left(\underline{p}.\underline{u}^* + \underline{\underline{P}} : \underline{\underline{v}}^*\right) d\Gamma = \int_{\partial\Omega} \left(\underline{p}.\underline{u}^* + \underline{\underline{P}}_t : \nabla_t \underline{u}^* + \underline{\underline{P}}_n : \underline{\underline{v}}_n^* + \underline{\underline{P}}_t : \left(\underline{\underline{v}}_t^* - \nabla_t \underline{u}^*\right)\right) d\Gamma \tag{A.8}$$

An integration by parts on $\partial\Omega$, assuming the surface is smooth enough and devoid of edges, yields the following expression:

$$\int_{\Omega} \left(\underline{\underline{\sigma}} : \nabla \underline{u}^* + \underline{\underline{\tau}} : \left(\underline{\underline{v}}^* - \nabla \underline{u}^*\right) + \overline{\Sigma} \therefore \nabla \underline{\underline{v}}^*\right) d\Omega = \int_{\partial\Omega} \left(\underline{s}.\underline{u}^* + \underline{P}_n.\underline{v}_n^* + \underline{\underline{P}}_t : \left(\underline{\underline{v}}_t^* - \nabla_t \underline{u}^*\right)\right) d\Gamma \tag{A.9}$$

where $\underline{s} = \underline{p} - \mathrm{div}_t \underline{\underline{P}}_t$, div_t being the operator divergence on the surface $\partial\Omega$. The balance equations of that modeling read:

$$\mathrm{div}\overline{\Sigma} - \tau = 0 \tag{A.10}$$

$$\mathrm{div}\left(\sigma - \tau\right) = 0 \tag{A.11}$$

and the boundary conditions are:

$$\overline{\Sigma}.\underline{n} = \underline{\underline{P}} \tag{A.12}$$

$$\left(\sigma - \tau\right).\underline{n} = \underline{s} + \mathrm{div}_t \left(\underline{\underline{P}}_t\right) \tag{A.13}$$

Eq. A.12 can be split into:

$$\left(\overline{\Sigma}.\underline{n}\right).\underline{n} = \underline{P}_n \tag{A.14}$$

$$\left(\overline{\Sigma}.\underline{n}\right)_t = \underline{\underline{P}}_t \tag{A.15}$$

Assuming $\underline{\underline{v}}^* = \nabla \underline{u}^*$, which entails that $\underline{\underline{v}}_t^* = (\nabla \underline{u}^*)_t = \nabla_t \underline{u}^*$ on $\partial\Omega$, in the equation (A.9) yields:

$$\int_{\Omega} (\underline{\underline{\sigma}} : \nabla \underline{u}^* + \overline{\Sigma} \therefore \nabla^2 \underline{u}^*) d\Omega = \int_{\partial\Omega} (\underline{s}.\underline{u}^* + \underline{T}.D\underline{u}^*) d\Gamma \tag{A.16}$$

which is the weak formulation of the equilibrium of a second gradient continuum.

References

[1] R. Peerlings, T. Massart, M. Geers, A thermodynamically motivated implicit gradient damage framework and its application to brick masonry cracking, Computer methods in applied mechanics and engineering 193 (30) (2004) 3403–3417.

[2] G. Jouan, P. Kotronis, F. Collin, Using a second gradient model to simulate the behaviour of concrete structural elements, Finite Elements in Analysis and Design 90 (0) (2014) 50 – 60. doi:http://dx.doi.org/10.1016/j.finel.2014.06.002.
URL http://www.sciencedirect.com/science/article/pii/S0168874X14001085

[3] C. Comi, S. Mariani, U. Perego, An extended fe strategy for transition from continuum damage to mode i cohesive crack propagation, International Journal for Numerical and Analytical Methods in Geomechanics 31 (2) (2007) 213–238.

[4] M. Jirasek, T. Zimmermann, Embedded crack model. part ii: Combination with smeared cracks, International Journal for Numerical Methods in Engineering 50 (6) (2001) 1291–1305.

[5] S. Cuvilliez, F. Feyel, E. Lorentz, S. Michel-Ponnelle, A finite element approach coupling a continuous gradient damage model and a cohesive zone model within the framework of quasi-brittle failure, Computer Methods in Applied Mechanics and Engineering 237 (2012) 244–259.

[6] P. Germain, The method of virtual power in continuum mechanics. part 2: Microstructure, SIAM Journal on Applied Mathematics 25 (3) (1973) 556 – 575. doi:http://dx.doi.org/10.1137/0125053.

[7] R. Mindlin, N. Eshel, On first strain-gradient theories in linear elasticity, International Journal of Solids and Structures 4 (1) (1968) 109 – 124. doi:http://dx.doi.org/10.1016/0020-7683(68)90036-X.

[8] R. Mindlin, Second gradient of strain and surface-tension in linear elasticity, International Journal of Solids and Structures 1 (4) (1965) 417 – 438. doi:http://dx.doi.org/10.1016/0020-7683(65)90006-5.

[9] E. Lorentz, A mixed interface finite element for cohesive zone models, Computer Methods in Applied Mechanics and Engineering 198 (2) (2008) 302–317.

[10] M. Bruggi, P. Venini, Modeling cohesive crack growth via a truly-mixed formulation, Computer Methods in Applied Mechanics and Engineering 198 (47) (2009) 3836–3851.

[11] G. Wells, L. Sluys, A new method for modelling cohesive cracks using finite elements, International Journal for Numerical Methods in Engineering 50 (12) (2001) 2667–2682.

[12] A. A. Griffith, Vi. the phenomena of rupture and flow in solids, Philosophical transactions of the royal society of London. Series A, containing papers of a mathematical or physical character 221 (582-593) (1921) 163–198.

[13] P.-E. Bernard, N. Moës, N. Chevaugeon, Damage growth modeling using the thick level set (tls) approach: Efficient discretization for quasi-static loadings, Computer Methods in Applied Mechanics and Engineering 233 (2012) 11–27.

[14] R. Chambon, D. Caillerie, N. E. Hassan, One-dimensional localisation studied with a second grade model, European Journal of Mechanics - A/Solids 17 (4) (1998) 637 – 656. doi:http://dx.doi.org/10.1016/S0997-7538(99)80026-6.

[15] R. Chambon, D. Caillerie, T. Matsuchima, Plastic continuum with microstructure, local second gradient theories for geomaterials: localization studies, International Journal of Solids and Structures 38 (46–47) (2001) 8503 – 8527. doi:http://dx.doi.org/10.1016/S0020-7683(01)00057-9.

[16] R. Chambon, J. Moullet, Uniqueness studies in boundary value problems involving some second gradient models, Computer Methods in Applied Mechanics and Engineering 193 (27) (2004) 2771–2796.

[17] T. Matsushima, R. Chambon, D. Caillerie, Second gradient models as a particular case of microstructured models: a large strain finite elements analysis, Comptes Rendus de l'Académie des Sciences-Series IIB-Mechanics-Physics-Astronomy 328 (2) (2000) 179–186.

[18] T. Matsushima, R. Chambon, D. Caillerie, Large strain finite element analysis of a local second gradient model: application to localization, International journal for numerical methods in engineering 54 (4) (2002) 499–521.

[19] P. Bésuelle, R. Chambon, F. Collin, Switching deformation modes in post-localization solutions with a quasibrittle material, Journal of Materials and Structures 1 (2006) 1115–1134.

[20] P. Kotronis, R. Chambon, J. Mazars, F. Collin, Local second gradient models and damage mechanics: application to concrete, 11th international conference on fracture, turin, italy, org. icf, cd, paper 5712, 2005, pp. 20–25.

[21] M. Soufflet, G. Jouan, P. Kotronis, F. Collin, Using a penalty term to deal with spurious oscillations in second gradient finite elements, International Journal of Damage Mechanics 28 (3) (2019) 346–366.

[22] P. Kotronis, S. Al Holo, P. Bésuelle, R. Chambon, Shear softening and localization: Modelling the evolution of the width of the shear zone, Acta Geotechnica 3 (2) (2008) 85–97. doi:10.1007/s11440-008-0061-4. URL http://dx.doi.org/10.1007/s11440-008-0061-4

[23] Y. Sieffert, S. Al Holo, R. Chambon, Loss of uniqueness of numerical solutions of the borehole problem modelled with enhanced media, International Journal of Solids and Structures 46 (17) (2009) 3173–3197.

[24] R. Fernandes, C. Chavant, R. Chambon, A simplified second gradient model for dilatant materials: Theory and numerical implementation, International Journal of Solids and Structures 45 (20) (2008) 5289 – 5307.

doi:http://dx.doi.org/10.1016/j.ijsolstr.2008.05.032.
URL http://www.sciencedirect.com/science/article/pii/S0020768308002205

[25] F. Collin, R. Chambon, R. Charlier, A finite element method for poro mechanical modelling of geotechnical problems using local second gradient models, International journal for numerical methods in engineering 65 (11) (2006) 1749–1772.

[26] S. Rolshoven, Nonlocal plasticity models for localized failure, Ph.D. thesis, École Polytechnique fédérale de Lausanne (2003).

[27] P. Kotronis, Stratégies de modélisation de structures en béton soumises à des chargements sévères, Habilitation à diriger des recherches, Université Joseph-Fourier-Grenoble I, http://tel.archives-ouvertes.fr/tel-00350461 (2008).

[28] G. Jouan, Modélisation numérique de la localisation des déformations dans le béton avec un modèle de second gradient, Ph.d., Ecole Centrale de Nantes, Université de Liège (cotutelle), http://bictel.ulg.ac.be/ETD-db/collection/available/ULgetd-11042014-112001/ (7 2014).

[29] M. Jirásek, S. Rolshoven, Localization properties of strain-softening gradient plasticity models. part i: Strain-gradient theories, International Journal of Solids and Structures 46 (11-12) (2009) 2225–2238.

[30] C. Giry, F. Dufour, J. Mazars, Stress-based nonlocal damage model, International Journal of Solids and Structures 48 (25) (2011) 3431–3443.

[31] A. Simone, H. Askes, L. Sluys, Incorrect initiation and propagation of failure in non-local and gradient-enhanced media, International Journal of Solids and Structures 41 (2) (2004) 351 – 363.

[32] Z. Wang, L. H. Poh, A homogenized localizing gradient damage model with micro inertia effect, Journal of the Mechanics and Physics of Solids 116 (2018) 370–390.

[33] D. Timofeev, E. Barchiesi, A. Misra, L. Placidi, Hemivariational continuum approach for granular solids with damage-induced anisotropy evolution, Mathematics and Mechanics of Solids 26 (5) (2021) 738–770.

[34] B. Pardoen, S. Levasseur, F. Collin, Using local second gradient model and shear strain localisation to model the excavation damaged zone in unsaturated claystone, Rock Mechanics and Rock Engineering 48 (2) (2015) 691–714.

[35] A. Van den Eijnden, P. Bésuelle, F. Collin, R. Chambon, J. Desrues, Modeling the strain localization around an underground gallery with a hydro-mechanical double scale model; effect of anisotropy, Computers and Geotechnics 85 (2017) 384–400.

[36] F. Collin, P. Kotronis, B. Pardoen, Numerical modelling of multiphysics couplings and strain localization, Alert Geomaterials Doctoral School, Modelling of instabilities and bifurcation in Geomechnics,

editors Jean Sulem, Ioannis Stefanou, Euripides Papamichos, Manolis Veveakis, 2016, pp. 247–291, http://alertgeomaterials.eu/publications/.

[37] S. Cuvilliez, Passage d'un modèle d'endommagement continu régularisé a un modèle de fissuration cohésive dans le cadre de la rupture quasi-fragile, Ph.D. thesis, Mines ParisTech (2012).

[38] F. Cazes, Construction et implémentation de lois cohésives extrinsèques, Phd, INSA de Lyon (2010). URL https://www.theses.fr/2010ISAL0075

[39] A. Simone, L. Sluys, The use of displacement discontinuities in a rate-dependent medium, Computer Methods in Applied Mechanics and Engineering 193 (27) (2004) 3015–3033.

[40] A. Simone, G. Wells, L. Sluys, From continuous to discontinuous failure in a gradient-enhanced continuum damage model, Computer Methods in Applied Mechanics and Engineering 192 (41) (2003) 4581–4607.

[41] S. Forest, R. Sievert, Elastoviscoplastic constitutive frameworks for generalized continua, Acta Mechanica 160 (1-2) (2003) 71–111.

[42] R. Mindlin, Micro-structure in linear elasticity, Archive for Rational Mechanics and Analysis 16 (1) (1964) 51–78.

[43] J. Li, A micromechanics-based strain gradient damage model for fracture prediction of brittle materials - part i: Homogenization methodology and constitutive relations, International Journal of Solids and Structures 48 (24) (2011) 3336–3345.

[44] J. Li, T. Pham, R. Abdelmoula, S. Song, C. Jiang, A micromechanics-based strain gradient damage model for fracture prediction of brittle materials – part ii: Damage modeling and numerical simulations, International Journal of Solids and Structures 48 (24) (2011) 3346 – 3358.

[45] Y. Yang, A. Misra, Micromechanics based second gradient continuum theory for shear band modeling in cohesive granular materials following damage elasticity, International Journal of Solids and Structures 49 (18) (2012) 2500–2514.

[46] F. Dell'Isola, G. Sciarra, S. Vidoli, Generalized hooke's law for isotropic second gradient materials, Proceedings of the Royal Society A: Mathematical, Physical and Engineering Sciences 465 (2107) (2009) 2177–2196.

[47] O. Zienkiewicz, R. Taylor, The finite element method for solid and structural mechanics, Butterworth-Heinemann, 2005.

[48] A. Zervos, P. Papanastasiou, I. Vardoulakis, A finite element displacement formulation for gradient elastoplasticity, International Journal for Numerical Methods in Engineering 50 (6) (2001) 1369–1388. doi:10.1002/1097-0207(20010228)50:6<1369::AID-NME72>3.0.CO;2-K.
URL http://dx.doi.org/10.1002/1097-0207(20010228)50:6<1369::AID-NME72>3.0.CO;2-K

[49] P. Fischer, J. Mergheim, P. Steinmann, On the c1 continuous discretization of non-linear gradient elasticity: A comparison of nem and fem based on bernstein–bézier patches, International Journal for Numerical Methods in Engineering 82 (10) (2010) 1282–1307.

[50] D. Caillerie, Second gradient linéaire et séries de fourier, personal communication, University Grenoble Alpes (2013).

[51] K. Enakoutsa, J. Leblond, Numerical implementation and assessment of the glpd micromorphic model of ductile rupture, European Journal of Mechanics-A/Solids 28 (3) (2009) 445–460.

[52] J. Shu, W. King, N. Fleck, Finite elements for materials with strain gradient effects, International Journal for Numerical Methods in Engineering 44 (3) (1999) 373–391.

[53] D. Boffi, F. Brezzi, M. Fortin, et al., Mixed finite element methods and applications, Vol. 44, Springer, 2013.

[54] M. Gantier, Modélisation numérique robuste et fiable de la fissuration des roches et des interfaces, Ph.d., Université Grenoble Alpes (2021).

[55] L. Placidi, A. Misra, E. Barchiesi, Two-dimensional strain gradient damage modeling: a variational approach, Zeitschrift für angewandte Mathematik und Physik 69 (3) (2018).

[56] L. Placidi, A. Misra, E. Barchiesi, Simulation results for damage with evolving microstructure and growing strain gradient moduli, Continuum Mechanics and Thermodynamics 31 (4) (2019) 1143–1163.

[57] L. Placidi, E. Barchiesi, Energy approach to brittle fracture in strain-gradient modelling, Proceedings of the Royal Society A: Mathematical, Physical and Engineering Sciences 474 (2210) (2018) 20170878.

[58] J. Mazars, Application de la mécanique de l'endommagement au comportement non linéaire et à la rupture du béton de structure, thèse de doctorat d'état de l'Université Paris VI (1984).

[59] P. Bésuelle, Implémentation d'un nouveau type d'élément fini dans le code lagamine pour une classe de lois á longueur interne, Tech. rep., Laboratoire Sols, Solides Structures, Grenoble, France, rapport d'activité (Mai 2003).

[60] F. Cazes, M. Coret, A. Combescure, A two-field modified Lagrangian formulation for robust simulations of extrinsic cohesive zone models, Computational Mechanics 51 (2013) 865–884. doi:10.1007/s00466-012-0763-1.

[61] R. Radovitzky, A. Seagraves, M. Tupek, L. Noels, A scalable 3d fracture and fragmentation algorithm based on a hybrid, discontinuous galerkin, cohesive element method, Computer Methods in Applied Mechanics and Engineering 200 (1) (2011) 326–344.

[62] G. Camacho, M. Ortiz, Computational modelling of impact damage in brittle materials, International Journal of solids and structures 33 (20) (1996) 2899–2938.

[63] F. Souza, D. Allen, Modeling failure of heterogeneous viscoelastic solids under dynamic/impact loading due to multiple evolving cracks using a two-way coupled multiscale model, Mechanics of Time-Dependent Materials 14 (2) (2010) 125–151.

[64] N. Moès, T. Belytschko, Extended finite element method for cohesive crack growth, Engineering Fracture Mechanics 69 (7) (2002) 813–833.

[65] E. Dvorkin, A. Cuitiño, G. Gioia, Finite elements with displacement interpolated embedded localization lines insensitive to mesh size and distortions, International Journal for Numerical Methods in Engineering 30 (3) (1990) 541–564.

[66] M. Jirásek, Comparative study on finite elements with embedded discontinuities, Computer Methods in Applied Mechanics and Engineering 188 (1) (2000) 307–330.

[67] S. Alam, Experimental study and numerical analysis of crack opening in concrete, Ph.D. thesis, Ecole Centrale de Nantes (ECN), https://tel.archives-ouvertes.fr/tel-00669877 (2011).

[68] S. Alam, P. Kotronis, A. Loukili, Crack propagation and size effect in concrete using a non-local damage model, Engineering Fracture Mechanics 109 (2013) 246–261.